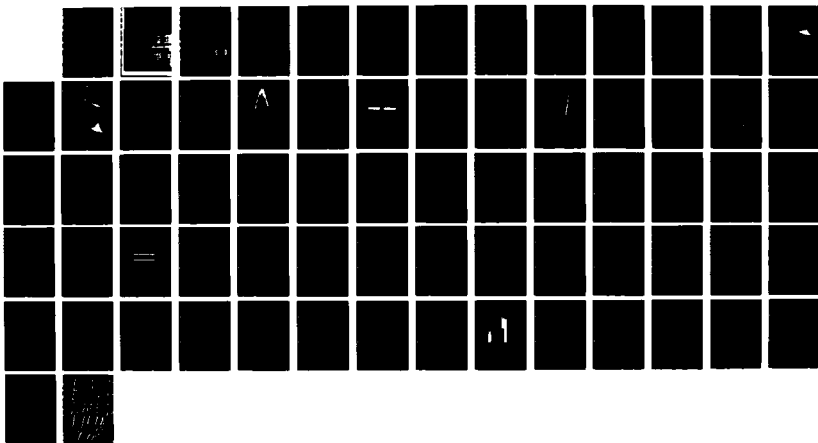AD-A194 238   ELECTRO-OPTIC TECHNIQUES FOR VERY LARGE SCALE   1/1
                INTEGRATED INTERCONNECTS(U) ORTEL CORP ALHAMBRA CA
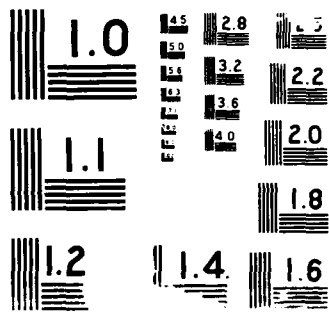   K Y LAU ET AL 20 APR 88 DAAH01-87-C-0983

UNCLASSIFIED   F/G 20/6   NL

AD-A194 238

of Contract:	September 1, 1987
tion Date:	March 1, 1988
d:	September 1, 1987-March
tigator:	Dr. Israel Ury

88 4 26 038

"Electro-Optic Techniques for Very Large
Scale Integrated Interconnects"

Final Report

Submitted by: Ortel Corporation
                                   2015 W. Chestnut St.
                                   Alhambra, CA 91803

Effective Date of Contract: September 1, 1987

Contract Expiration Date: March 1, 1988

Reporting Period: September 1, 1987-March 1, 1988

Principal Investigator: Dr. Israel Ury
                                   (818) 281-3636

                        April 20, 1988   **DTIC**
                                              S **ELECTE** **D**
                                                APR 2 6 1988

                                                 H

                            Unclassified

The views and conclusions contained in this document are those of the authors
and should not be interpreted as representing the official policies, either
expressed or implied, of the Defense Advanced Research Projects Agency or the
U.S. Government.

SECURITY CLASSIFICATION OF THIS PAGE

1

REPORT DOCUMENTATION PAGE

A194 257

1a. REPORT SECURITY CLASSIFICATION	1b. RESTRICTIVE MARKINGS
Unclassified	

2a. SECURITY CLASSIFICATION AUTHORITY	3. DISTRIBUTION / AVAILABILITY OF REPORT
	Approved for public release;
2b. DECLASSIFICATION / DOWNGRADING SCHEDULE	distribution unlimited.

4. PERFORMING ORGANIZATION REPORT NUMBER(S)	5. MONITORING ORGANIZATION REPORT NUMBER(S)

6a. NAME OF PERFORMING ORGANIZATION	6b OFFICE SYMBOL (If applicable)	7a. NAME OF MONITORING ORGANIZATION
Ortel Corporation	5U557	U.S. Army Missile Command

6c. ADDRESS (City, State, and ZIP Code)	7b. ADDRESS (City, State, and ZIP Code)
2015 W. Chestnut St.	AMSMI-PC-BFA/DARPA Project Office
Alhambra, CA 91803	Redstone Arsenal, AL 35898-5280

8a. NAME OF FUNDING / SPONSORING ORGANIZATION	8b. OFFICE SYMBOL (If applicable)	9. PROCUREMENT INSTRUMENT IDENTIFICATION NUMBER
DARPA	U31P40	DAAH01-87-C-0983

8c. ADDRESS (City, State. and ZIP Code)	10. SOURCE OF FUNDING NUMBERS			
	PROGRAM ELEMENT NO.	PROJECT NO.	TASK NO.	WORK UNIT ACCESSION NO.
1400 Wilson ave.				
Arlington, VA 22200				

11. TITLE (Include Security Classification)

Electro-Optic Techniques for Very Large Scale Integrated Interconnects

12. PERSONAL AUTHOR(S)
Lau, Kam Y., Kwong, Sze-Keung, Ury, Israel

13a. TYPE OF REPORT	13b. TIME COVERED	14. DATE OF REPORT (Year, Month, Day)	15. PAGE COUNT
Final	FROM 870901 TO 880301	880420	

16. SUPPLEMENTARY NOTATION

17.	COSATI CODES		18. SUBJECT TERMS (Continue on reverse if necessary and identify by block number)
FIELD	GROUP	SUB-GROUP	

19. ABSTRACT (Continue on reverse if necessary and identify by block number)

Superluminescent diodes with broad emission spectrum, which makes them insensitive to optical feedback and hence most suitable for massively interconnected systems, have been fabricated with an integrated modulator. The superluminescent has high emission power (up to 30mW) which makes possible systems with many levels of branchings. The modulator is based on carrier induced absorption and shows a very high modulation efficiency. In addition to device fabrication and experimental measurements which shows a direct modulation bandwidth beyond 1GHz, the static and dynamics of the superluminescent diode, with and without the integrated modulator, have been analyzed. It is shown that by using quantum well materials much improvement in modulation efficiency as well as bandwidths in the multigigahertz range can be accomplished.

20. DISTRIBUTION / AVAILABILITY OF ABSTRACT	21. ABSTRACT SECURITY CLASSIFICATION
☒ UNCLASSIFIED/UNLIMITED ☐ SAME AS RPT. ☐ DTIC USERS	Unclassified

22a. NAME OF RESPONSIBLE INDIVIDUAL	22b. TELEPHONE (Include Area Code)	22c. OFFICE SYMBOL

DD FORM 1473, 84 MAR   83 APR edition may be used until exhausted.   SECURITY CLASSIFICATION OF THIS PAGE
All other editions are obsolete.

CONTENT

1. Introduction

In recent years it has become clear that the coming generation of computers will require some form of optical interconnect, whether it be intrachip, chip-to-chip or board-to-board. Initially the interconnects will almost certainly be realized using optical fibers. Very significant technbological challenges are still present in the first generation of fiber interconnect schemes. Great progress has been made in developing very high speed lasers and photodiodes whose response extends beyond 10GHz and which has lasing thresholds below 1mA. However, there can be significant problems associated with laser sources in a massively interconnected network. First, the laser is a threshold device. That is, a certain amount of current is required to flow through the device before lasing occurs. If the laser is not biased in the lasing mode, the high speed characteristics are not realized. Therefore ordinarily, monitor photodiodes and automatic feedback power controlling circuits are needed for proper bias control of the laser. We have developed ultralow threshold (0.5mA) single quantum well lasers[1-3] to counter this problem. Secondly, lasers ordinarily require two mirrors to set up the lasing cavity. This is conventionally done by cleaving the chip to form the laser cavity. Since the optimum length for a laser cavity is generally on the order of $300\mu m$, it will severely confine the dimension of the chip to this dimension and will be a severe handicap in attempting to put electronic circuits monolithically

with the lasers. We have developed half-ring lasers and will continue to develop full ring lasers to counter this problem. Thirdly, since the distances involved in optical interconnect is rather short, multimode fibers are likely to be used for the reason of both cost and ease of assembly and it is well known that a highly coherent source used in a multimode fiber system can encounter modal noise[4]. In addition, optical feedback into the laser can greatly affect its noise properties due to the high coherence.

While work is on-going to solve the problems listed above, we adopt here a new line of attack in which a high power incoherent optical source is used. Such sources are known as superlumines-cent diodes (SLD), and were originally designed primary for use as sources for fiber sensors. In order to efficiently modulate the optical output we integrate a modulator monolithically to the SLD. Results of this investigation shows that the device holds great promises for countering all of the problems mentioned above and can become key elements in fiber-based optical interconnect systems.

2. Superluminescent diodes

2.1 Device design and construction

An SLD is characterized by high output power and low beam divergence similar to an injection laser, but with a broad

emission spectrum and low coherence similar to a light emitting diode. To obtain high output power from an SLD requires very high optical gain within the device, consequently suppression of lasing is a key concern. Several methods have been used to suppress lasing in lasers to obtain superluminescence , such as using an unpumped absorber [5], a proton implanted absorber [6], anti-reflection (AR) coating at the front facet [7-12] and an angled stripe [13,14]. In this program we studied SLD's based on a proven high power, high efficiency "window" type index guided buried heterostructure laser [15]. Lasing is suppressed for SLD operation by antireflection (AR) coating and by incorporating a rear absorber section. The resulting device emits high optical power (23 mW) in the SLD mode at low injection current ($\leq$ 140 mA). The spectral modulation depth is below 30% over the entire emission spectral bandwidth of 15 nm, with a symmetrical beam divergence (20°x40°) and a stable transverse mode. The symmetric far-field pattern allows efficient coupling into a single mode polarization preserving fiber with coupled power as high as 5 mW.

The structure of the SLD is shown in Fig. 1. It is based on the "window" buried heterostructure laser [15]. The buried heterostructure provides excellent current confinment, and therefore, low operating current for the SLD. This real index guiding laser structure also produces a stable single transverse mode output over a large range of operating current. The output region near the front facet is composed of a layer of unpumped

Fig. 1: Schematic diagram of the window buried heterostructure SLD.

Cr – Au

S$_i$O$_2$

Zn diffusion

p-GaAlAs

GaAlAs

n-GaAlAs

p-GaAlAs

n$^+$GaAs

AuGe-Ni-Au

pumped region

absorber

Cr-Au
n-GaAlAs

n-GaAlAs

n$^+$GaAs

p-GaAlAs

n-GaAlAs

p-GaAlAs

n-GaAlAs

n$^+$GaAs

KL80225C

GaAlAs which forms a transparent window thus averting catastrophic damage suffered by conventional GaAlAs devices at high power. An anti-reflection coating on the window facet minimizes feedback to the active region and simultaneously enhances optical output power from the front facet. An absorbing region at the back end of the active gain region absorbs radiation propagating away from the output end, thereby suppressing laser oscillation. The absorbing region is formed by shorting the p-n junction to ground in the rear section of the waveguide. This is an efficient method to increase the absorption of the waveguide by "draining" the photo-excited carriers to ground. Typical device dimensions are: length of the pumped region $L=250\mu m$; the grounded absorber region $l=150\mu m$; the gap between the pumped and the grounded absorber region $d=50\mu m$; and the window region, $t=5\mu m$.

2.2 Device Perfomance

(a) Light-Current Characteristics and Optical Spectra

The device characteristics were evaluated under three stages: (1) No AR coating and an open-circuit absorber; (2) AR coated and an open-circuit absorber; and (3) AR coated and a grounded absorber.

(1) No AR coating and an open-circuit absorber

The light-current characteristic of the device shows a double "threshold" as shown in Fig. 2. The light output was
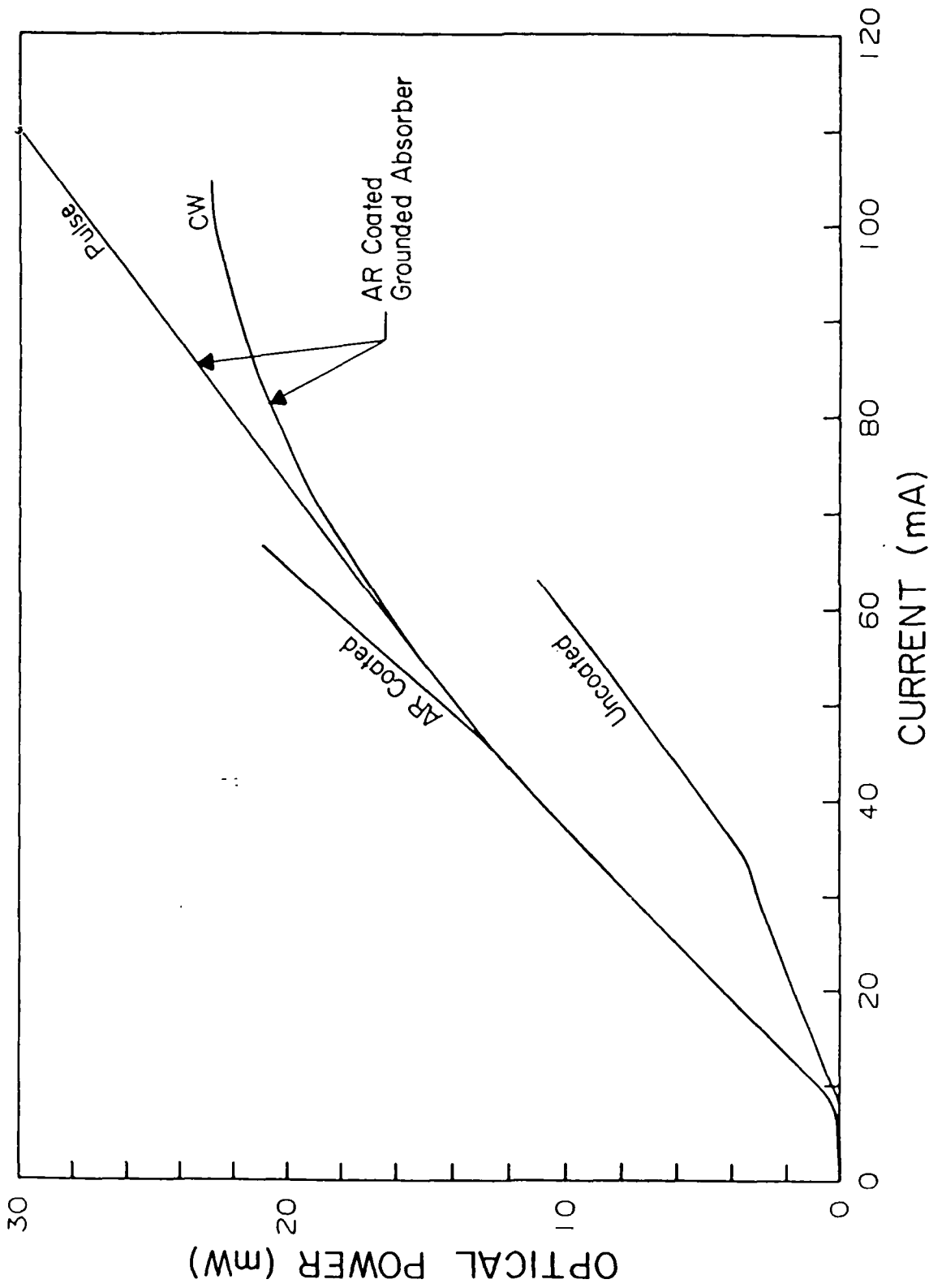
Fig. 2: Light versus current characteristics of an SLD in three cases: (1) uncoated and an open-circuit absorber, (2) AR coated and an open-circuit absorber, and (3) AR coated and a grounded absorber.

measured from the front facet (i.e. the side without the absorber). Referring to the curve for the device without AR coating in Fig. 2, the first threshold is interpreted as the onset of the superluminescent mode of operation. The emission spectrum shown in Fig. 3a displays a characteristic superluminescent structure. The spectral modulation, which is defined as $m=(I_{max}-I_{min})/(I_{max}+I_{min})$ at the peak of the spectrum, is less than 12%.

At the point of the "second threshold", which occurs at approximately 3 mW, distinct longitudinal modes emerge at the longer wavelength end of the superluminescent spectrum indicating lasing action, see Fig. 3b. At the same time, the optical output power from the rear facet (where the absorber is located) increases markedly. This is interpreted as the "burning through" of the absorber by the superluminescent radiation thus making laser oscillation between the facets possible. The equation relating the ouput power and the facet reflectivities is
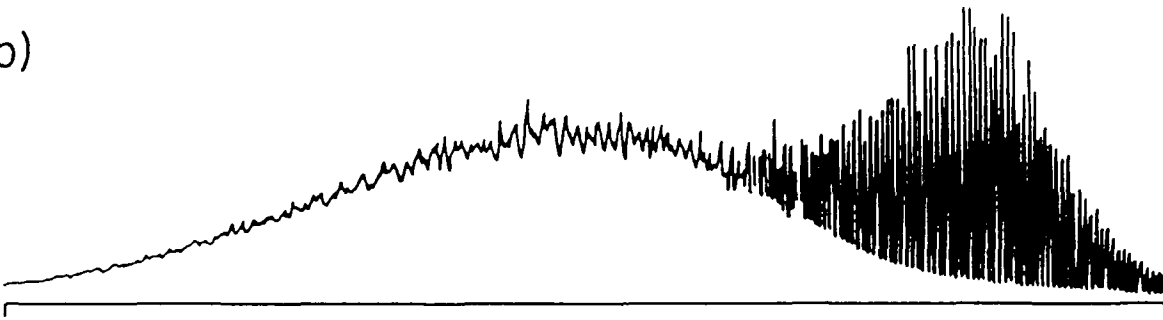
$$\frac{P_1}{P_2} = \sqrt{\frac{R_2 T_1}{R_1 T_2}} \qquad (1)$$

where P_1 and P_2 are the output power at the front and rear facets respectively. R_1, R_2, T_1, and T_2 are the reflectivity and the transmitivity at the front and rear facets respectively. The reflectivity of the uncoated window front facet was measured to be 18%. The reflectivity from the back facet is greatly reduced
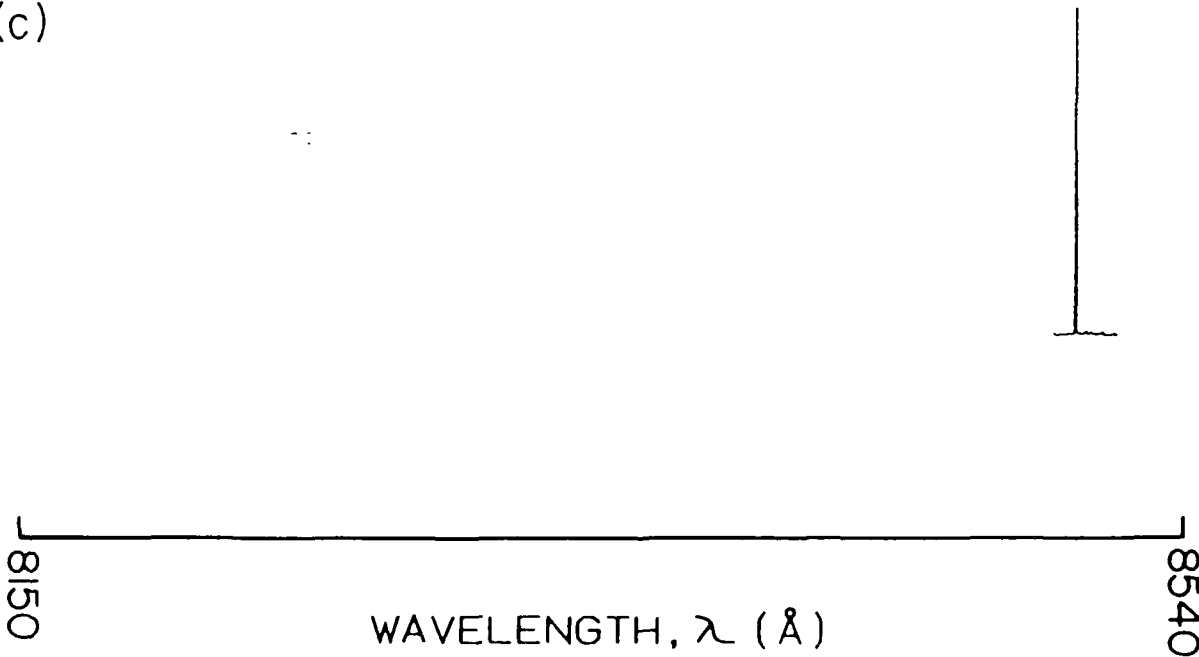
(a)

(b)

(c)

8150
8540

WAVELENGTH, λ (Å)

Fig. 3: (a), (b), and (c) are the spectra of the uncoated SLD at currents of 23, 35, and 47 mA, respectively.

by the absorber. As a result, we would expect a very large power ratio between the forward and backward travelling waves thus making it easier to burn through the absorber at relatively low power at the front. On further increase of pump current, a single lasing mode eventually dominates with a side-mode suppression ratio of >30 dB, see Fig. 3c. The lasing modes always occurs at the longer-wavelength end of the spectrum and is believed to occur there due to the lower absorption at the photon energies closer to the bandgap of the active region (band filling effect). The reason for the large degree of side-mode suppression is not clear and is under investigation.

(2) AR coated and an open-circuit absorber

By AR coating the front facet, the second threshold point is extended to approximately 14 mW at 50 mA, see Fig. 2. This can be understood from the reflectivity formula equation (1), - the amount of backward propagating light is reduced by an AR coating at the front facet, thus making it more difficult to burn through the absorber. The spectra of the AR coated SLD at currents of 40, 49, and 60 mA are shown in Figs. 3d, 3e,and 3f, respectively. Beyond the burn-through point, the spectrum shows distinct longitudinal modes as before, see Fig. 3F. The variation of the spectral modulation with injection current is shown in Fig. 4. Below the point of lasing, the spectral modulation of the SLD is between 12% to 14% and is relatively constant with current. Near the lasing threshold (at about 40 mA) the spectral modulation at
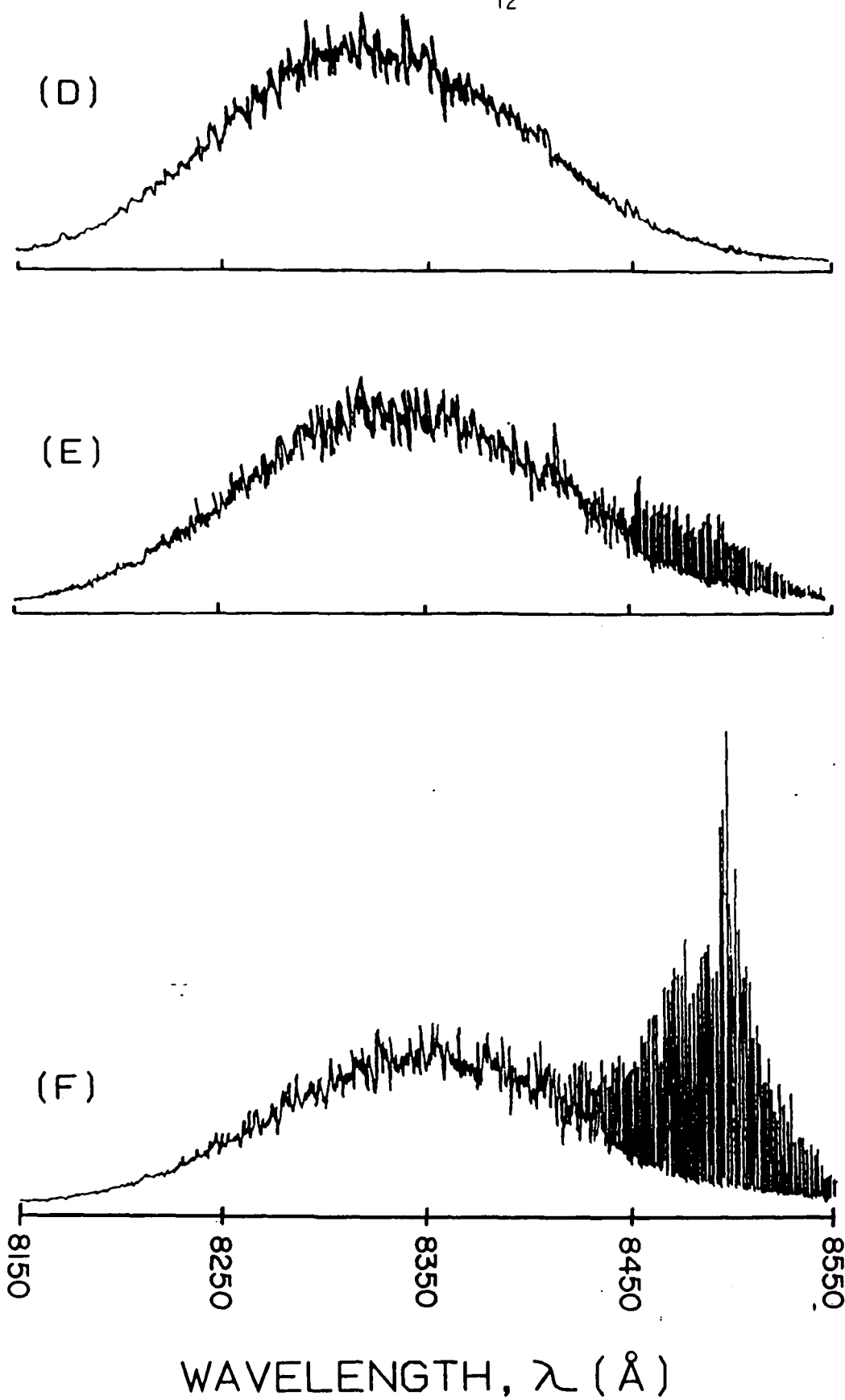
(D)

(E)

(F)

WAVELENGTH, λ (Å)

8150   8250   8350   8450   8550

Fig. 3: (d), (e), and (f) are the spectra of the AR coated SLD at currents of 40, 49, and 60 mA, respectively.
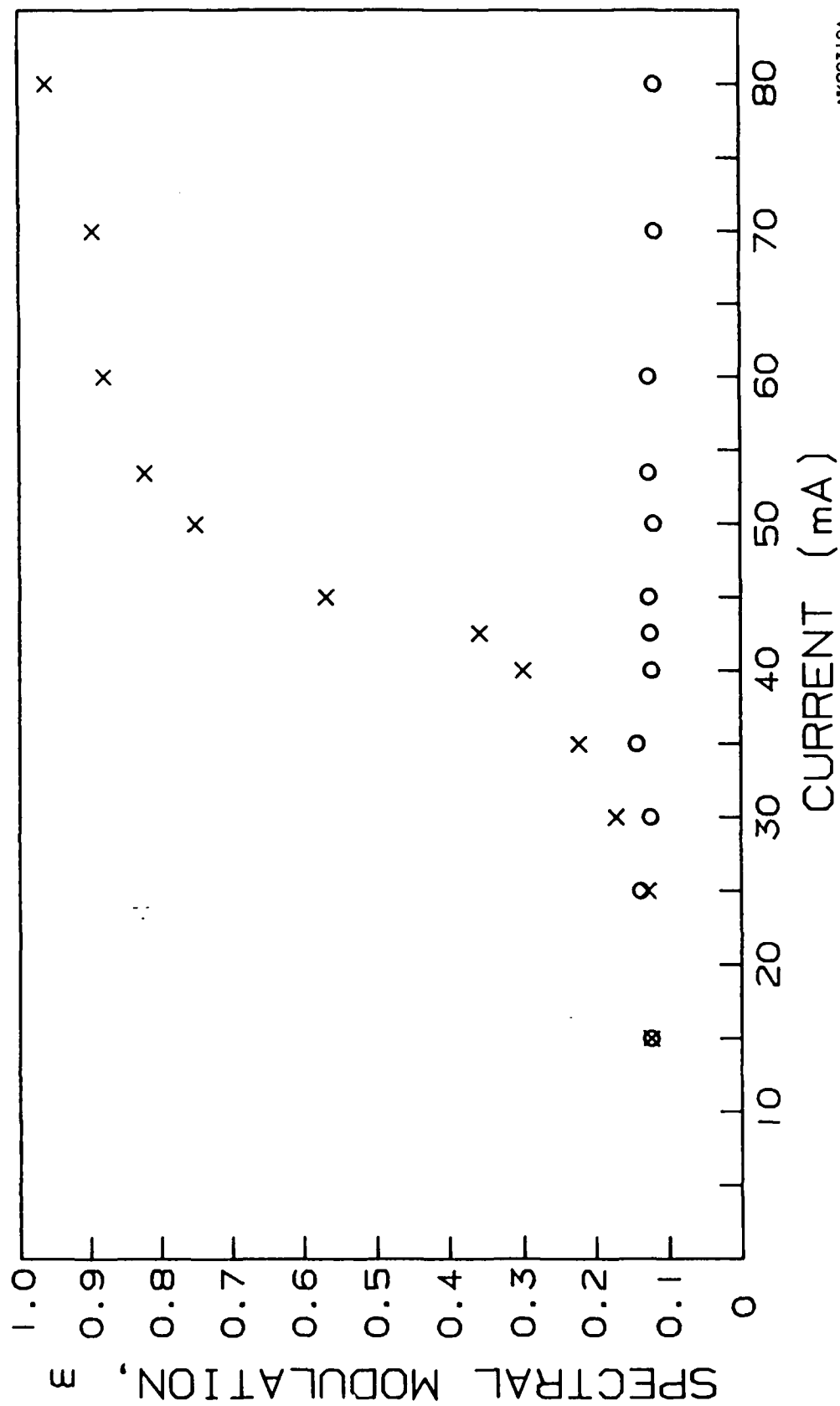
Fig. 4: The spectral modulation versus current at λ = 830 nm (o) and 850 nm (x).

NK80310A

the longer wavelengths (850nm) increases drastically. However, the spectral modulation at the non-lasing wavelengths (for example: 830nm) remains at about 12%. The spectral width of the emission is 20 nm at an output power of 14 mW.

(3) AR coated and grounded absorber

By shorting the p-n junction to ground in the absorber section, carriers cannot accumulate inside the absorber and hence burn-through is prevented. The light-current characteristics of the device is shown in Fig. 2. The device is capable of putting out 23 mW at 100 mA injection current. The pulsed light-current curve shows that the device can operate in SLD mode at least up to 30 mW. This implies that the CW output power of the device is limited by heating, since it is mounted junction side-up on a copper heat sink. With junction side down mounting, we expect the output power to be futher improved. The emission spectrum at 23 mW is shown in Fig. 5. The spectral width at FWHM is 20 nm. The estimated coherence length ($l_c = \lambda^2/\Delta\lambda$, where $\Delta\lambda$ is the FWHM spectral width) is $50\mu m$, which has been confirmed by an interferometric measurement (Fig. 6). The spectral modulation at the peak of the spectrum is less than 25%.

(b) Characteristics of the absorber

The I/V characteristics of the absorber with various pump currents were studied. The experimental set-up is shown in Fig. (7a). The light/current curve and the the corresponding curve on
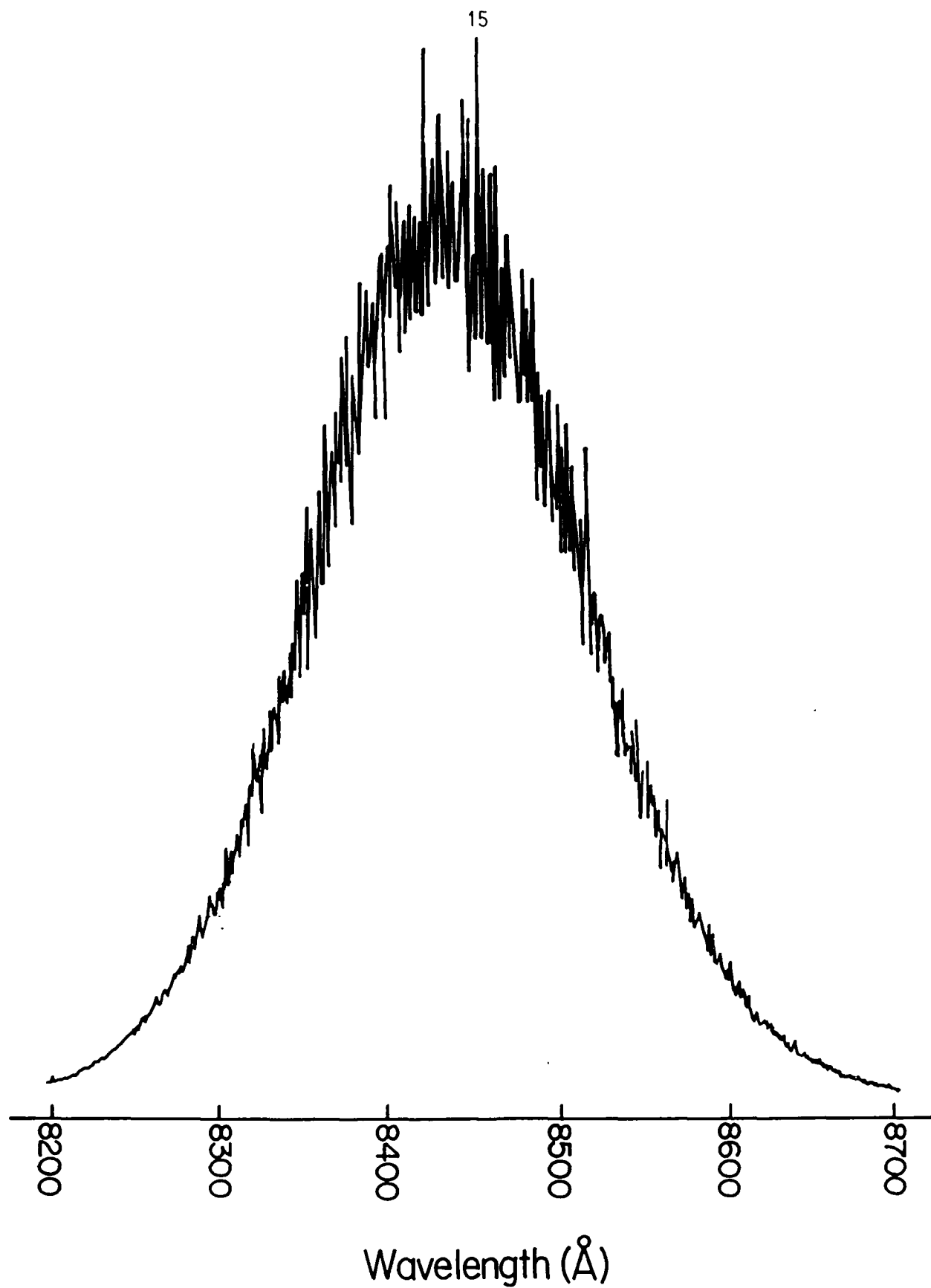
Fig. 5: The spectrum of an SLD with AR coating and a grounded absorber at 100 mA and 23 mW output power.
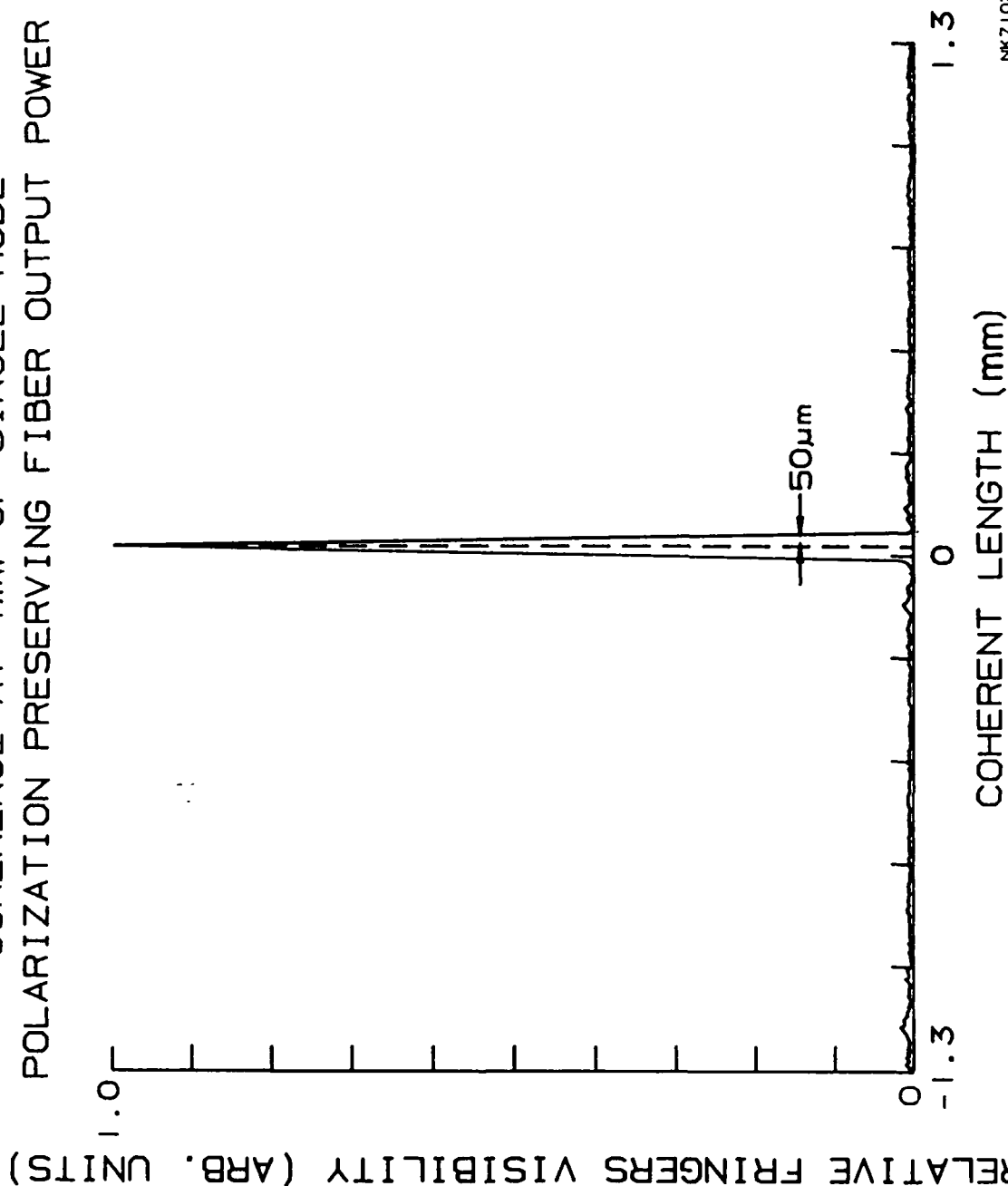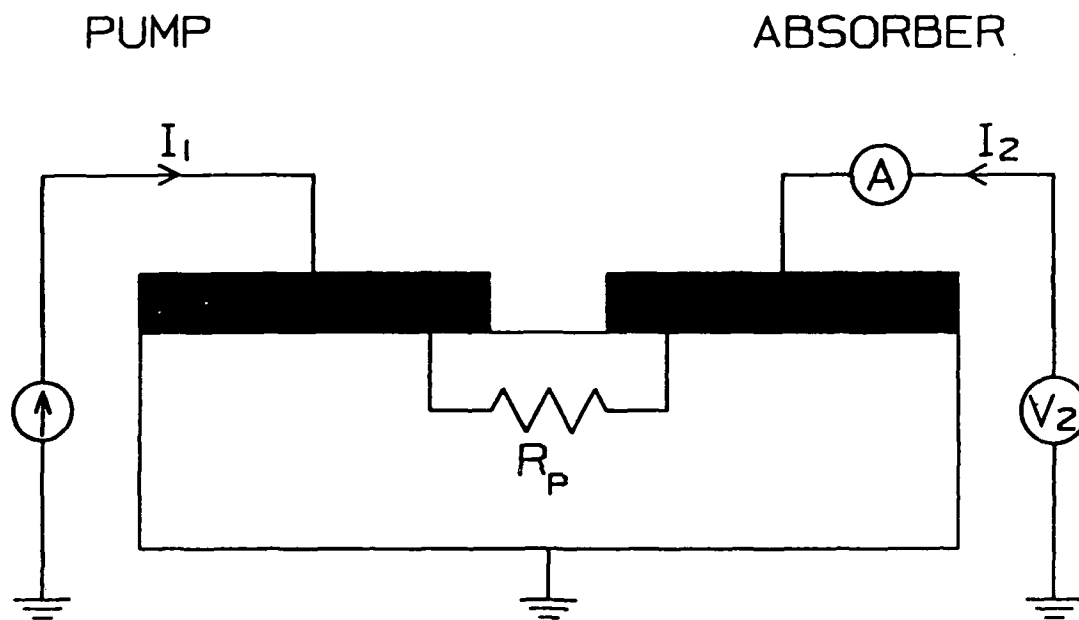
Fig. 6: Coherence at 4 mW of single mode polarization preserving fiber output power.

NK71120Z

Fig. 7: (a) Schematic diagram of the experiment to measure the I/V characteristics of the absorber.

absorber current I_2, versus pump current I_1, are shown in Fig. (7b). The voltage across the pump region is typically 2V when the pump current is above the threshold. The parasitic resistance R_p across the two contacts is measured to be 22.5 kΩ. Therefore the leakage current across the two contact pads is about 0.09mA which is negligible. Therefore we believe that the current I_2 is mainly due to photo-excited carriers being drained to the ground. The I/V characteristics of the absorber at various pump currents are shown in Fig. (7c). We noted that the absorber current only increases slightly with an applied negative bias voltage on the absorber, i.e. I_2 is saturated for $V_2 < 0$

(c) Far-field Characteristics

The far-field pattern of the SLD is shown in Fig. 8a and 8b. The spatial resolution of the apparatus used to measure the far-field pattern is 0.5°. The far-field full width at half maximum are 20° and 40° for scans parallel and perpendicular to the junction plane, respectively. The far-field pattern shows a smooth angular dependence which is another indication of the very low coherence of the SLD. There is no significant narrowing of the far field with increasing current, which suggests that the lateral mode behavior is dominated by real index guiding. The far-field pattern of a laser from the same wafer are also shown in Fig. 8c and 8d for comparison.
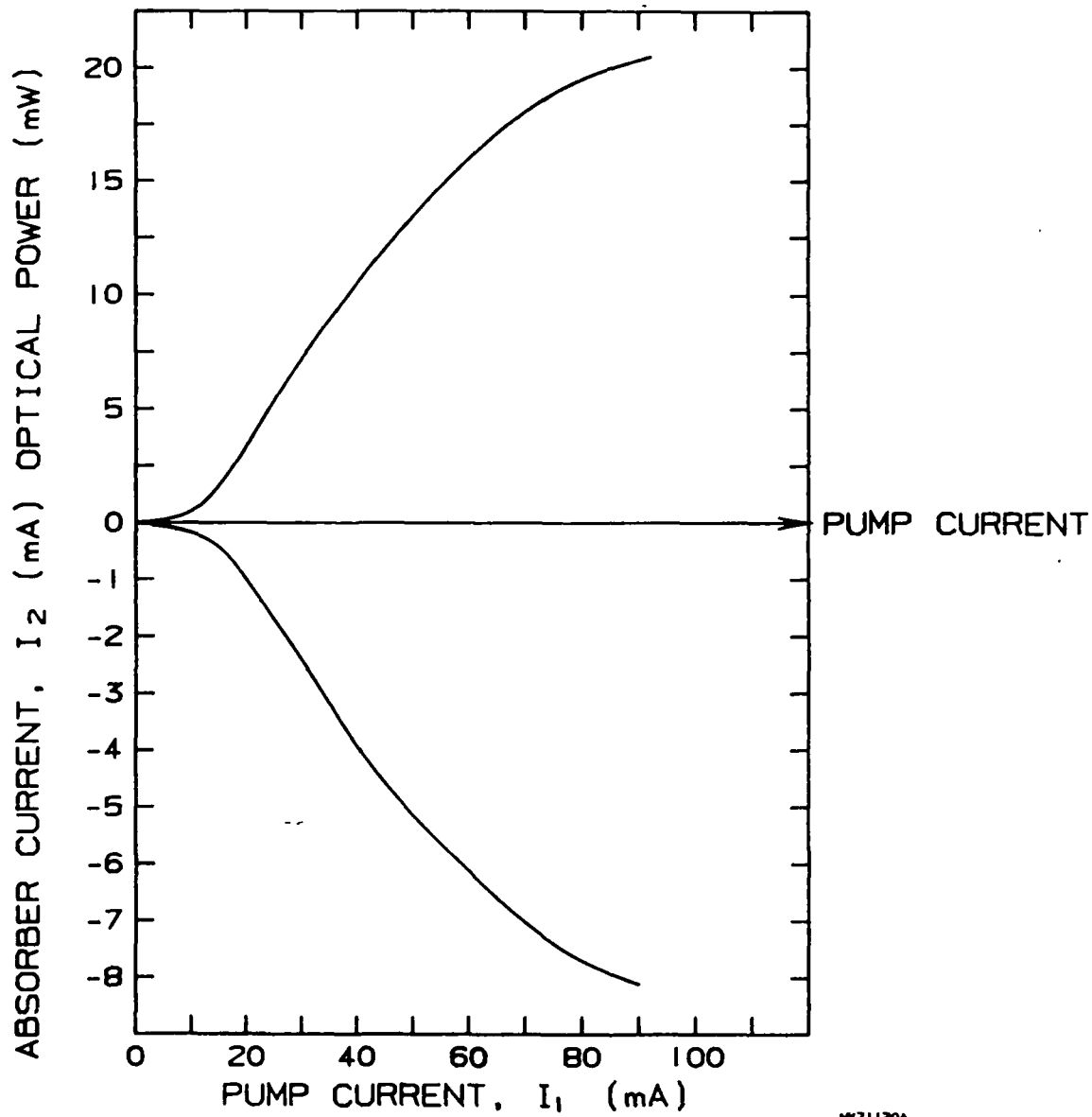
Fig. 7: (b) The light/current curve and the corresponding absorber current versus pump current curve.
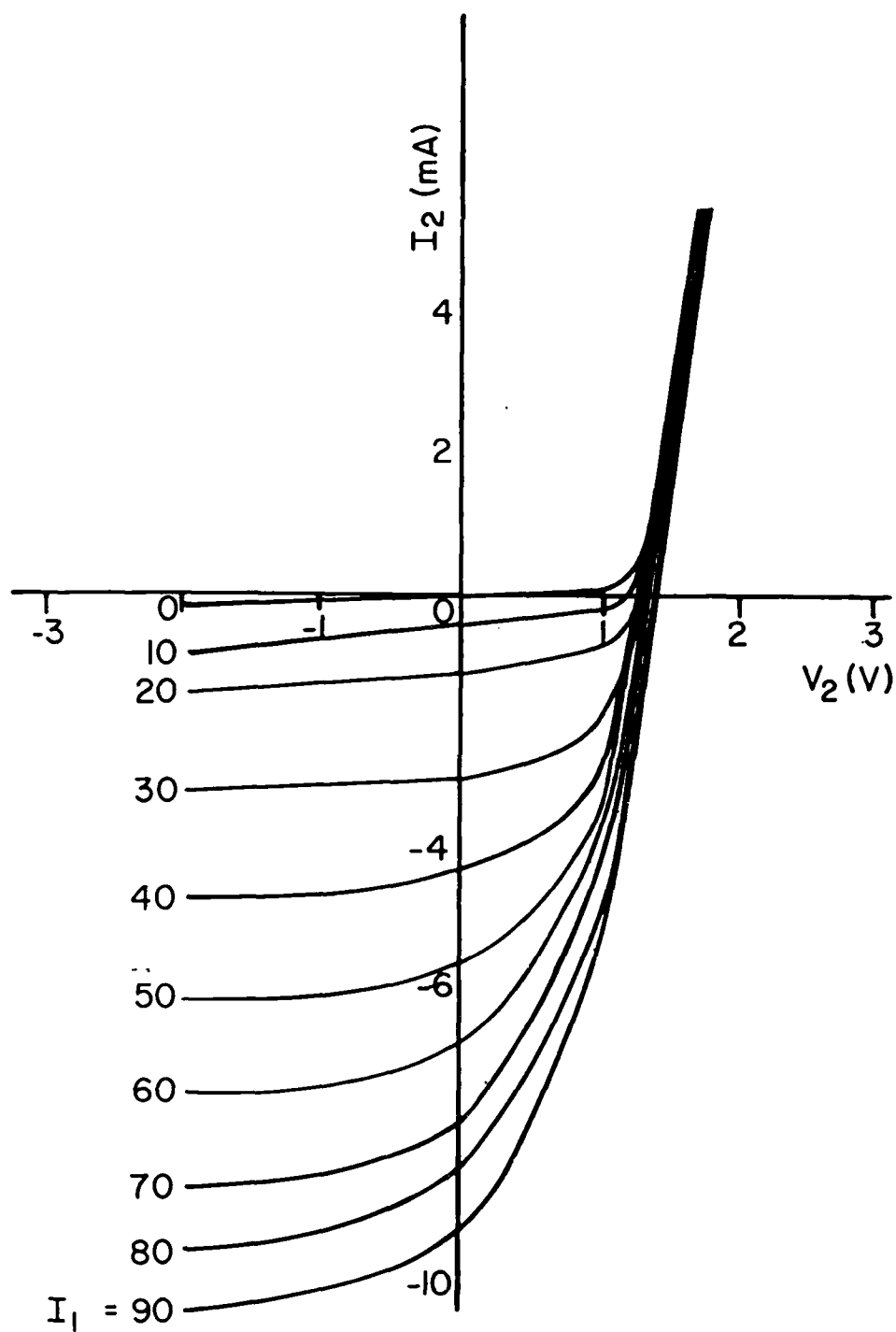
Fig. 7: (c) The I/V characteristics of the absorber at various pump currents.
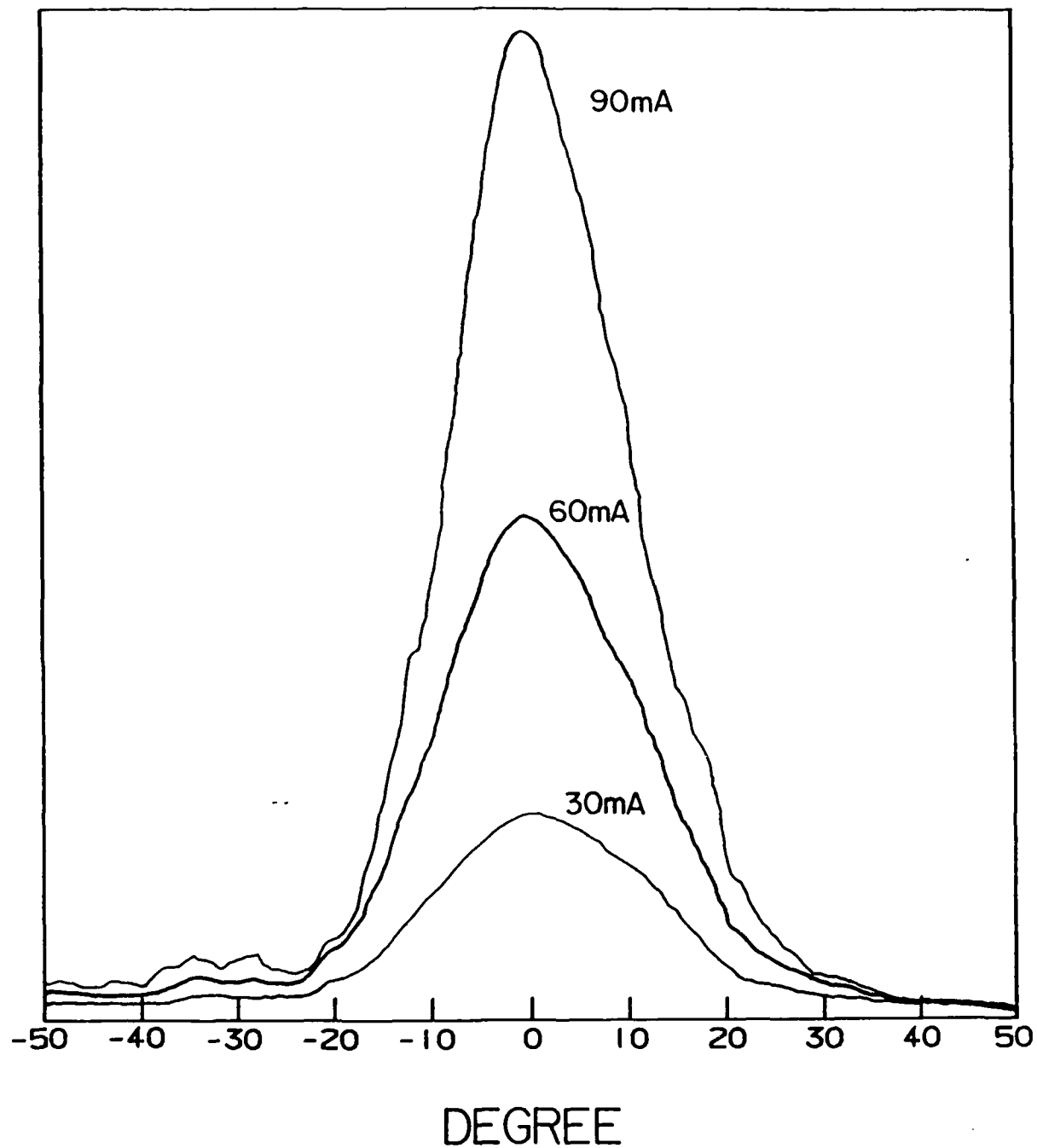
Fig. 8: (a) Far-field intensity distribution of the SLD parallel to the junction.
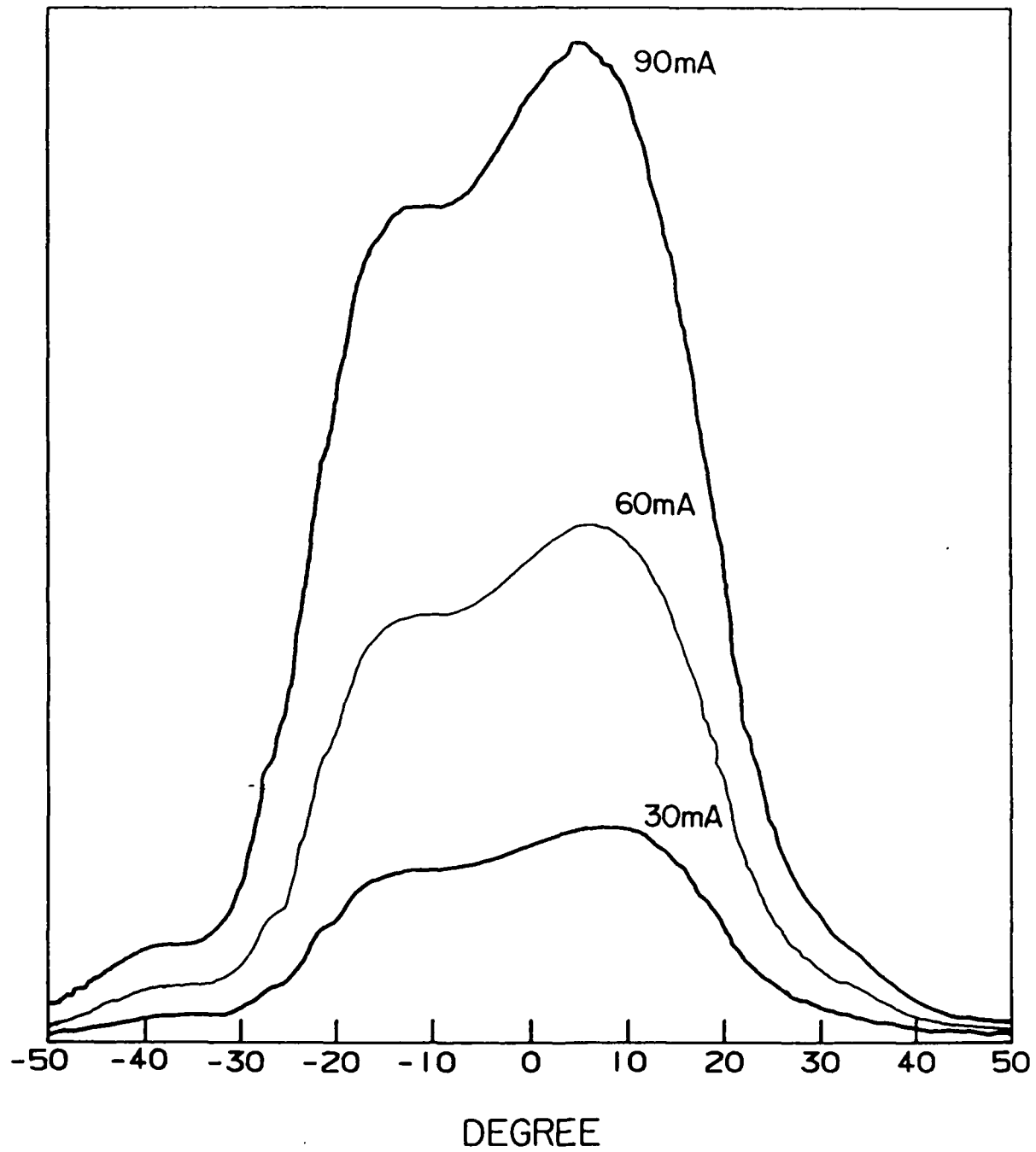
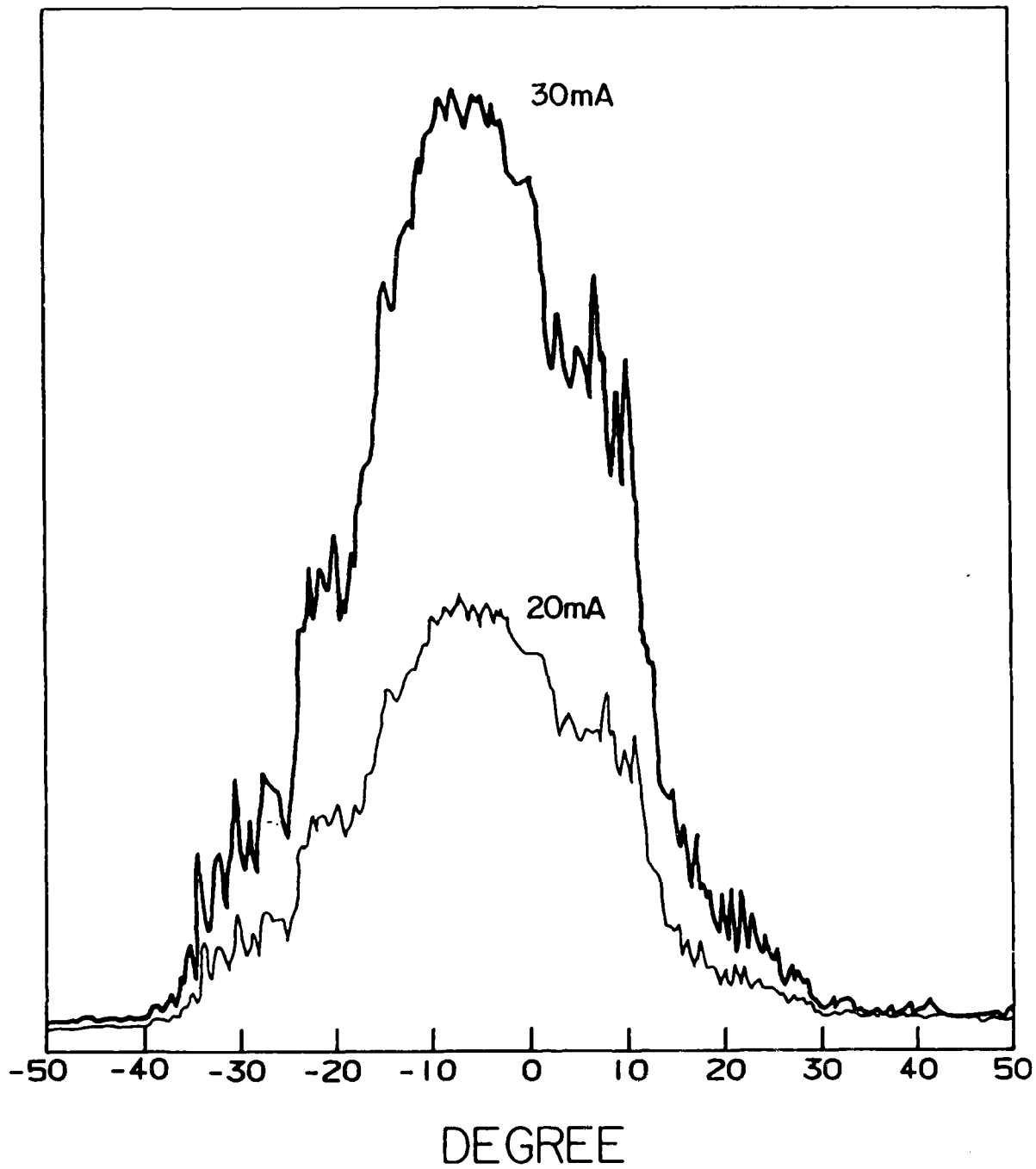Fig. 8: (b) Far-field intensity distribution of the SLD perpendicular to the junction.

Fig. 8: (c) Far-field pattern of a laser from the same wafer parallel to the junction.
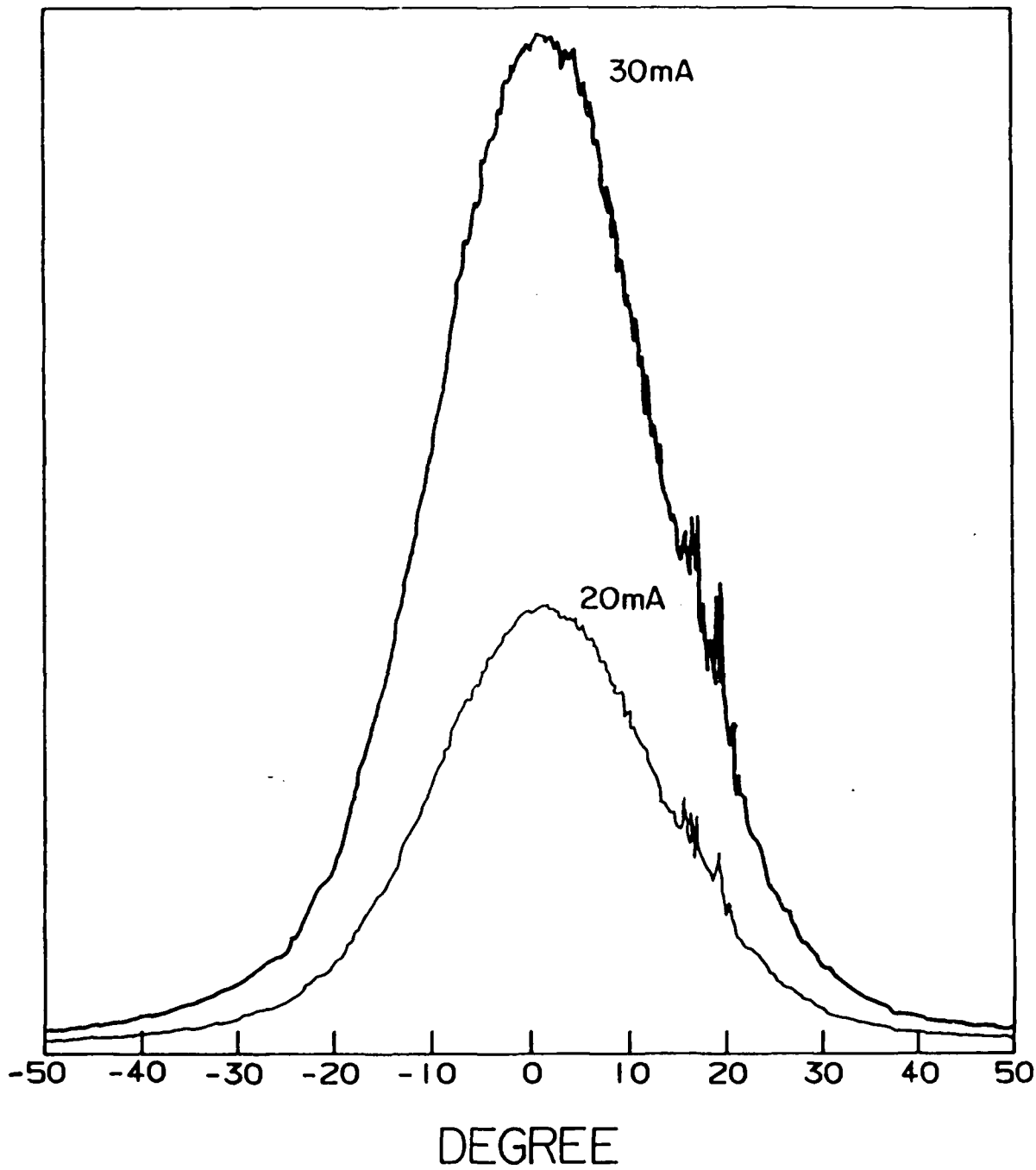
Fig. 8: (d) Far-field pattern of a laser from the same wafer perpendicular to the junction.
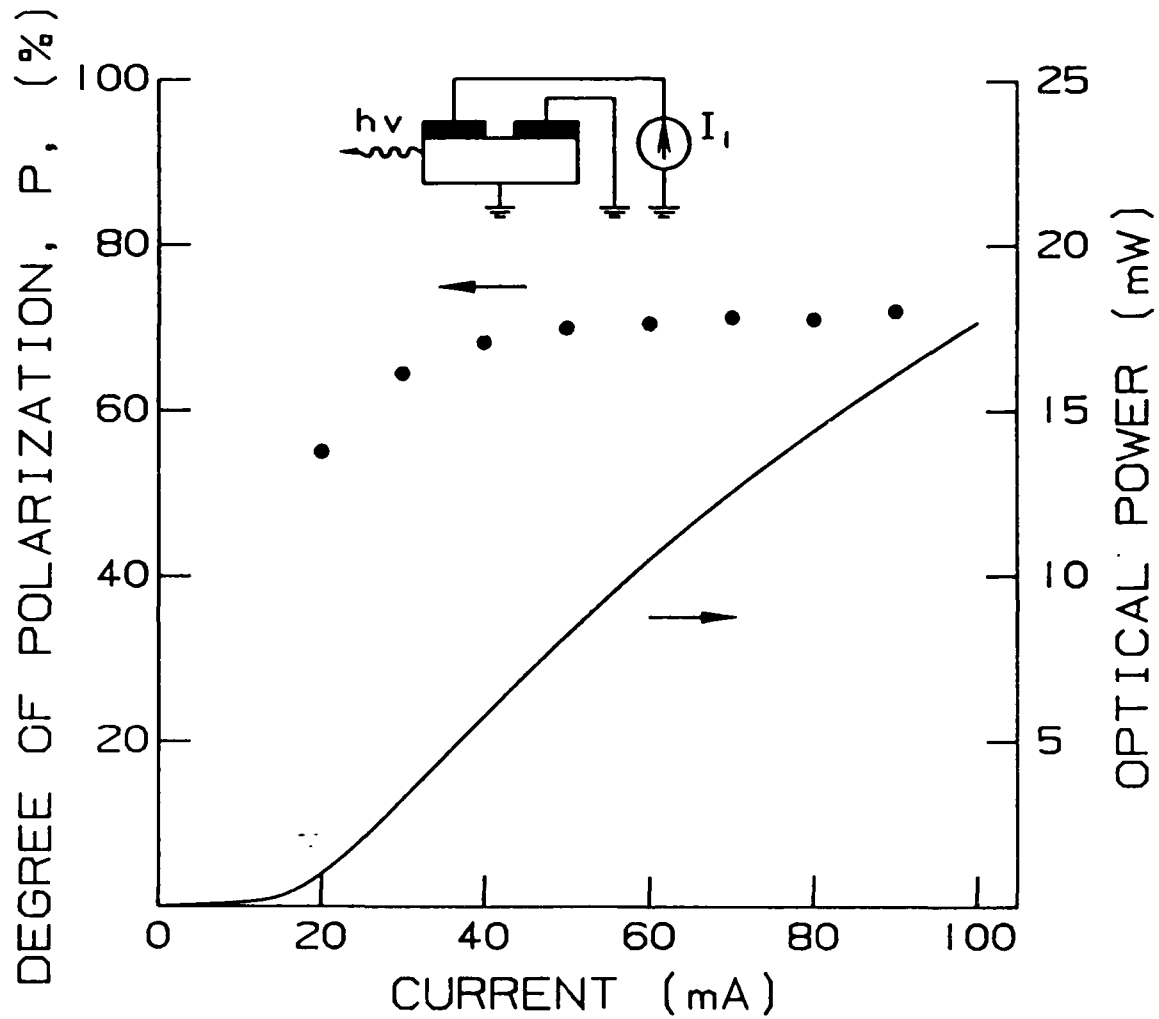
(d) Degree of Polarization

Since an SLD has less optical feedback than a laser, we expect the optical output from an SLD to be less linearly polarized than a laser. The degree of polarization from an SLD may be defined as $P=(I_{TE}-I_{TM})/(I_{TE}+I_{TM})$, where I_{TE} and I_{TM} are the intensity of the polarized light along and perpendicular to the junction plane, respectively. P=1 when all the power is in TE modes, and P=-1 when the radiation is in TM mode. The quantity, P, for both the SLD and a laser from the same wafer were measured for various currents. When the laser is operating above threshold, the degree of polarization is consistently higher than 97% which indicates that TE mode is the preferential oscillating mode, as expected (Fig. 9). The degree of polarization for the SLD with an open-circuit absorber varies from 45% to 80% for the current range of 10 mA to 80 mA (Fig. 9). The degree of polarization for an SLD with a grounded absorber is about 70% for current range from 30mA to 90mA (Fig. 10).

The spectra of the TE and TM modes are shown in Fig. 11. The spectral modulation for TE mode is larger than that for the TM mode, which indicates that the TE mode experiences a higher feedback from the facets. The peak of the TM mode spectrum is shifted about 5nm towards the shorter wavelength relative to that of the TE mode. Such shifting may be due to less optical confinement for the longer wavelength TM mode, hence higher penetration through the upper cladding and absorption by the
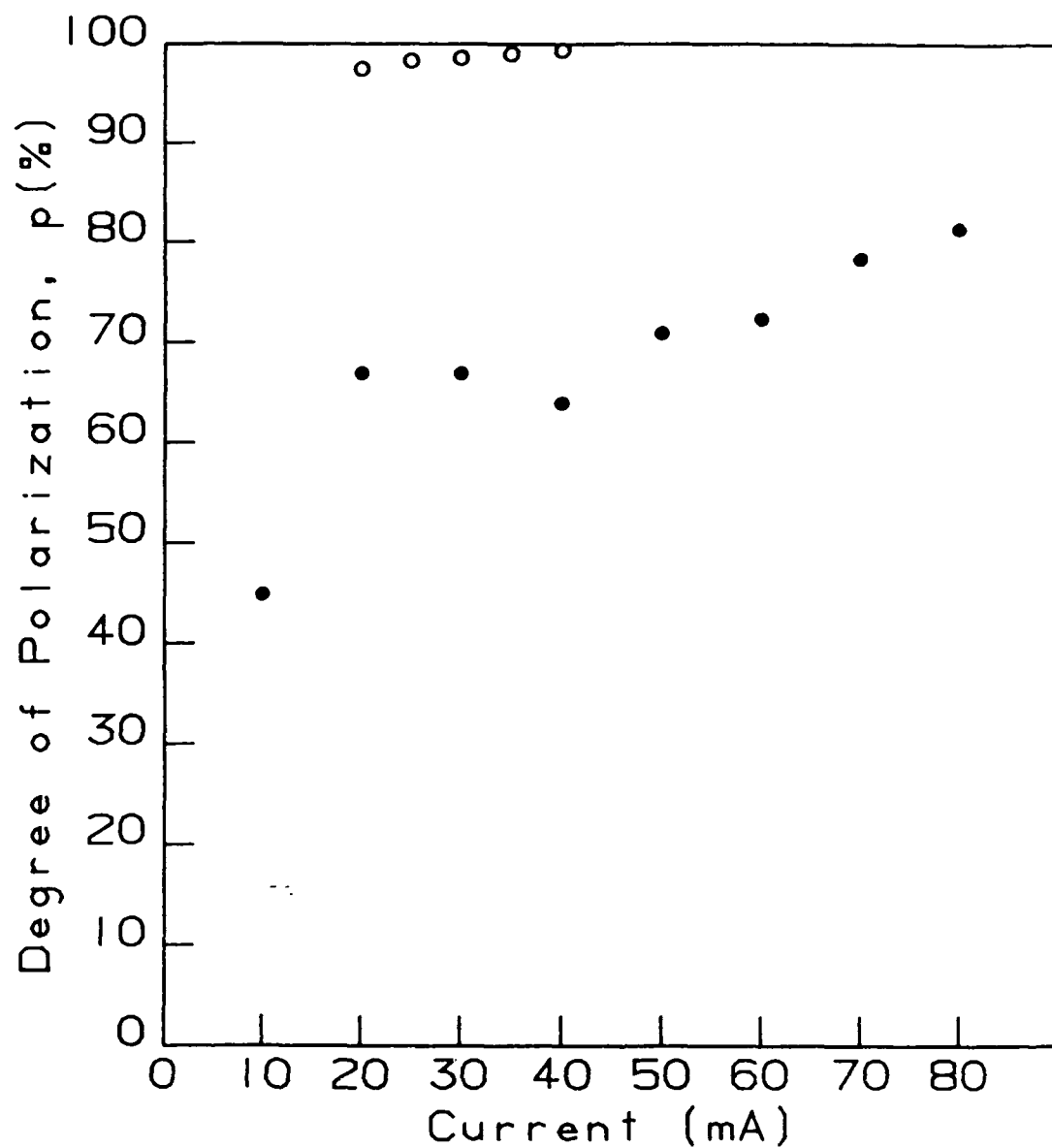
NK70707D

Fig. 9: Degree of polarization versus injection current: (·) for an SLD with AR coating and open absorber; (o) for laser from the same wafer.

Fig. 10: Degree of polarization versus injection current for an SLD with AR coating and a grounded absorber.
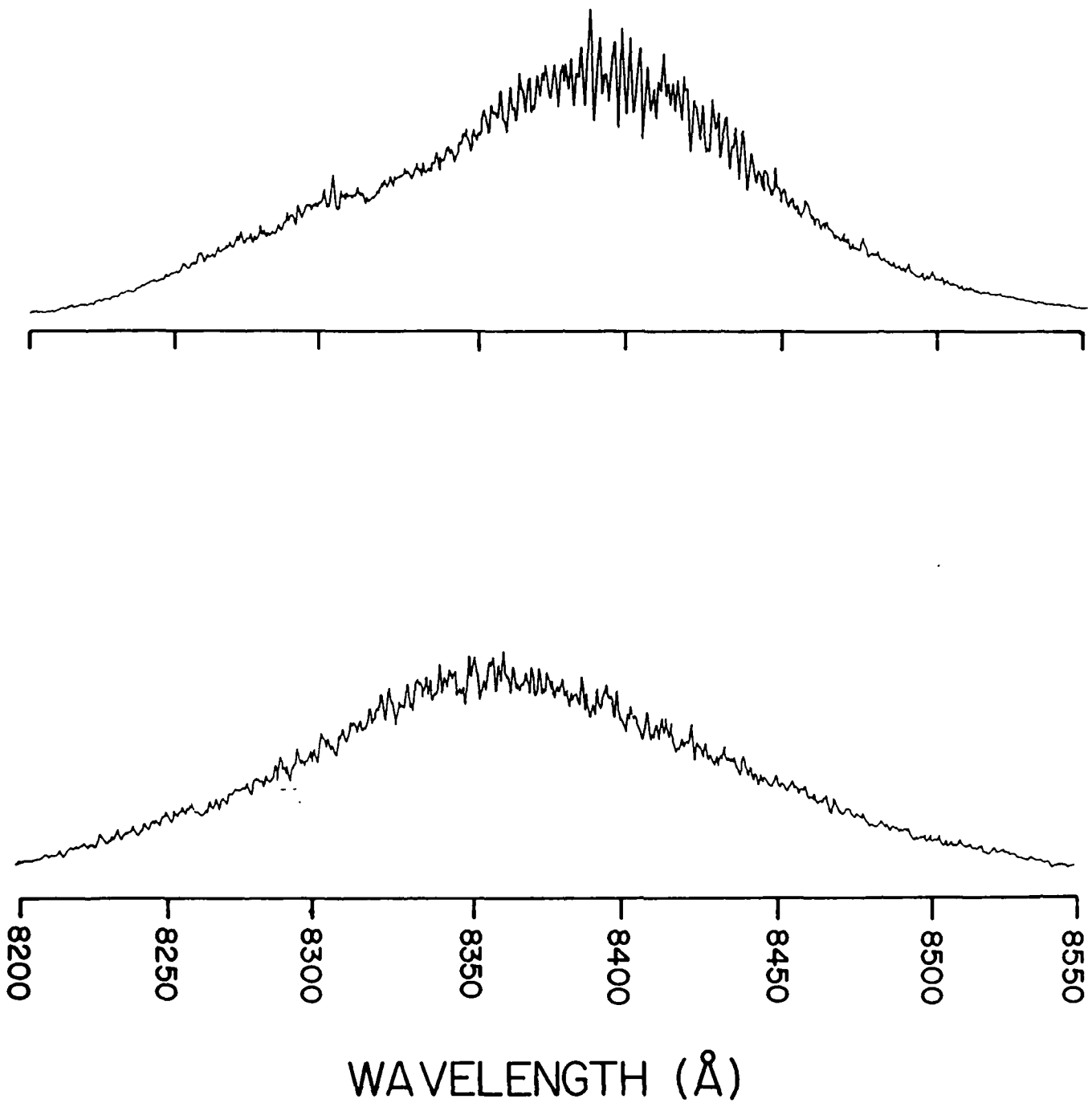
WAVELENGTH (Å)

Fig. 11: Optical spectra of an SLD with grounded absorber: TE mode (upper) and TM mode (lower).

metallization. For practical applications, such as gyroscopes, the SLD is coupled to a polarization preserving fiber. Therefore it is more desirable to have a highly linearly polarized SLD light source. From the above, polarizibility can be improved by making a thinner upper cladding layer.

2.3 Discussion

It is clear from the above analysis that the output power of the SLD increases and the spectral modulation decreases by reducing the facet reflectivity. The most effective method is to improve the AR-coating. We have constructed an optically monitored AR-coating system. The system performs an active in-line monitoring of the lasing spectrum of a laser in an electron beam evaporation system while coatings are being applied. Since the spectral width of the SLD is very wide (40 nm), the power contained in each unit wavelength is very small and hence the spectrometer output is quite noisy. This problem is aggravated by the fact that a large area fiber bundle (4 mm in diameter) is used to collect the laser output inside the vacuum chamber and only a small portion of the collected light is fed into the slit entrance of the spectrometer. The temporal fluctuations in the SLD spectrum also contribute to the difficulty in the measurment. Under these conditions, we can tell quite easily whether or not the diode is lasing but it is quite difficult to read the exact spectral modulation depth in

the SLD mode and a fine control of the coating thickness is not possible. An alternative to monitoring the spectrum is to monitor the quantum efficiency, i.e. the slope of the light/current curve. This method is under investigation.

3. Theoretical Model

3.1 The governing equations

The behavior of the superluminescent diode described above can be very accurately described by a theoretical model that takes into account the longitudinal distribution of photons and electrons along the length of the gain and absorber media. Referring to Fig. 12, we applied the coupled rate equations to the pumped and absorber region separately. They are shown as follow:

For the gain region:

$$\frac{1}{c}\frac{\partial X^+}{\partial t} + \frac{\partial X^+}{\partial z} = \kappa N X^+ + \frac{\beta}{c}\frac{N}{\tau_s} \tag{2a}$$

$$\frac{1}{c}\frac{\partial X^-}{\partial t} - \frac{\partial X^-}{\partial z} = \kappa N X^- + \frac{\beta}{c}\frac{N}{\tau_s} \tag{2b}$$

$$\frac{dN}{dt} = \frac{J}{eh} - \frac{N}{\tau_s} - \kappa c N\left(X^+ + X^-\right) \tag{2c}$$

For the absorbing region:

$$\frac{1}{c}\frac{\partial X^{+\prime}}{\partial t} + \frac{\partial X^{+\prime}}{\partial z} = \kappa\left(N' - N_o'\right)X^{+\prime} \tag{3a}$$
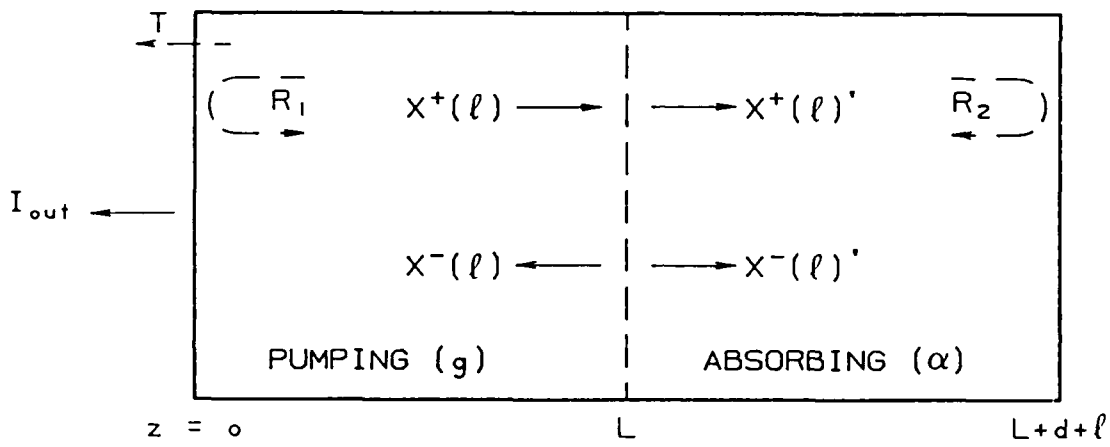
Fig. 12: Schematic diagram of the SLD for theoretical modeling.

$$\frac{1}{c}\frac{\partial X^{-}}{\partial t} - \frac{\partial X^{-}}{\partial z} = \kappa\left(N^{'} - N_{o}^{'}\right)X^{-} \tag{3b}$$

$$\frac{dN^{'}}{dt} = -\frac{N^{'}}{\tau_{s}} - \kappa c\left(N^{'} - N_{o}^{'}\right)\left(X^{+} + X^{-}\right) \tag{3c}$$

where the primed quantities indicate variables in the absorbing region, X^{+} and X^{-} are the forward and backward propagating photon densities (which are proportional to the light intensities), N is the majority carrier density, N_{o} is the effective minority carrier density which takes the place of the lower state population density in an ordinary two-level laser, and its value determines the bias current density required for optical transparency, c is the group velocity of the waveguide mode, κ is the gain costant in cm^{-1}/(unit carrier density), β is the fraction of spontaneous emission captured by the waveguide, τ_{s} is the spontaneous recombination lifetime of the carriers, z is the distance along the active medium with z=0 at the front facet of the SLD, J is the pump current density, e is the electronic charge and h the thickness of the active region in which the carriers are confined.

To simplify the calculation, the term $\kappa N_{o}X^{+}$ is not included in Eq. (2). We estimated the current required for transparency is about 2/5 of the threshold current. Therefore the theoretical curves shown in the following are shifted by 4 mA to account for the term $\kappa N_{o}X^{+}$. The term $\beta N/c\tau_{s}$ is also neglected in Eq. (3).

Eq. (2) and (3) are to be solved subject to the boundary conditions:

$$R_1 X^-(0) = X^+(0) \tag{4}$$

$$R X^+(L) = X^-(L) \tag{5}$$

$$X^+(L) = X^+(L)', \, X^-(L) = X^-(L)' \tag{6}$$

$$R_2 X^+(s)' = X^-(s)' \tag{7}$$

where L is the length of the pumping region, s=L+d+l is the length of the SLD, d is the unpumped gap between the pumping and the grouned absorber region, l is the length of the grounded absorber, R_1 is the reflectivity at the output facet, R_2 is the reflectivity at the rear facet, and R is the ratio of the light goes into the pumping region to the light goes into the absorber at z=L.

3.2 Solution for output power

Let us first solve Eq. (2) with the boundary conditions Eqs. (4) and (5). In steady state, Eqs. (2a) and (2b) reduce to

$$\frac{dX^+}{dz} = \kappa N \left(X^+ + \frac{\beta}{\kappa c \tau_s} \frac{1}{} \right) \tag{8a}$$

$$\frac{dX^-}{dz} = -\kappa N \left(X^- + \frac{\beta}{\kappa c \tau_s} \frac{1}{} \right) \tag{8b}$$

Assume the solutions have the form [14]

$$X^+(z) + \frac{\beta}{\kappa c \tau_s} = \frac{a}{\kappa c \tau_s} e^{u(z)} \tag{9a}$$

$$X^-(z) + \frac{\beta}{\kappa c \tau_s} = \frac{a}{\kappa c \tau_s} e^{-u(z)} \tag{9b}$$

where a and u(z) are quantities to be determined. In terms of these substitutions,

$$\frac{dX^+}{dz} = \frac{a}{\kappa c \tau_s} e^{u(z)} \frac{du(z)}{dz} \tag{10}$$

From Eq. (8a)

$$\frac{dX^+}{dz} = \kappa N \frac{a}{\kappa c \tau_s} e^{u(z)} \tag{11}$$

comparing Eqs. (10) and (11),

$$\frac{du}{dz} = \kappa N \tag{12}$$

The carrier density, derived from Eq. (2c) is

$$N = \frac{J/eh}{1/\tau_s + \kappa c \left(X^+ + X^-\right)} \tag{13}$$

Substitute Eq. (13) into (12), we obtain

$$\frac{du}{dz} = \frac{g}{(1-2\beta) + a\left(e^{u(z)} + e^{-u(z)}\right)} \tag{14}$$

where

$$g = \frac{\kappa J \tau_s}{eh} \tag{15}$$

Integrate Eq. (14), we get

$$(1-2\beta)(u(L) - u(0)) + a\left(e^{u(L)} - e^{u(0)}\right) - a\left(e^{-u(L)} - e^{-u(0)}\right) = gL \tag{16}$$

From the boundary conditions Eqs. (4) and (5) and the substitution in Eq. (9),

$$e^{u(0)} = \frac{(1-R_1)\beta + \sqrt{\beta^2(1-R_1)^2 + 4R_1 a^2}}{2a} \tag{17}$$

and

$$e^{u(L)} = \frac{(R-1)\beta + \sqrt{\beta^2(R-1)^2 + 4Ra^2}}{2Ra} \tag{18}$$

From Eqs. (16)-(18), we can calculate the unknown a, u(0) and u(L) for given R. The optical power output is

$$I(out) = TX^-(0) = T\left(\frac{ae^{-u(0)} - \beta}{\kappa c \tau_s}\right) \tag{19}$$

where T is the transmittivity at the output facet.

We used the similar procedure to solve the Eqs. (3a)-(3c). Let

$$X^+(z)' = \frac{b}{\kappa c \tau_s} e^{v(z)} \tag{20a}$$

$$X^-(z)' = \frac{b}{\kappa c \tau_s} e^{-v(z)} \tag{20b}$$

Substitute Eq. (20) into Eqs. (3a) and (3b), we get

$$\frac{dv}{dz} = -\frac{\kappa N_o}{1 + b\left(e^{v(z)} + e^{-v(z)}\right)} \tag{21}$$

Integrate Eq. (21), we obtain

$$v(s) - v(L) + b\left(e^{v(s)} - e^{-v(s)} - e^{v(L)} + e^{-v(L)}\right) + \kappa N_o(s-L) = 0 \tag{22}$$

From Eq. (20a),

$$v(L) = \ln\left(\frac{\kappa c \tau_s}{b} X^*(L)^{\cdot}\right)$$
(23)

From boundary condition Eqs. (5) and (6),

$$R = \frac{X^-(L)^{\cdot}}{X^*(L)^{\cdot}} = e^{-2v(L)}$$
(24)

Substitute Eq. (23) into Eq. (24), we get

$$R = \left(\frac{b}{\kappa c \tau_s} \frac{1}{X^*(L)^{\cdot}}\right)^2$$
(25)

Substitute Eqs. (23)-(25) into Eq. (22), we obtain

$$X^*(L)^{\cdot} = -\frac{\alpha(s-L) + \frac{1}{2}\ln(R_2 R)}{\kappa c \tau_s \sqrt{R}\left(1/\sqrt{R_2} - \sqrt{R_2} - 1/\sqrt{R} + \sqrt{R}\right)}$$
(26)

where $\alpha = \kappa N_0$.

Therefore I(out) can be obtained by simultaneously solving Eqs. (9), (16)-(19), and (26).

Theoretical curves of the output power versus current for the uncoated, AR coated, and grounded absorber are shown in Fig. 13. The parameters used in these calculations are $\alpha - 400cm^{-1}$ [16], β =0.071, L=250μm, d=50μm, l=150μm, R_1(uncoated)=0.18, R_1(AR-coated)=0.018, R_2=0.1, R(grounded absorber)=10^{-4}. T_1(uncoated)=0.7, and T_1(AR-coated)=0.97. The theoretical curves match quite well with the experimental curves shown in Fig. 2. A key in matching the data is the use of an apparently very high value for β, the spontaneous emission factor. It was found that smaller values of β give much lower superluminescence power below the burn-through
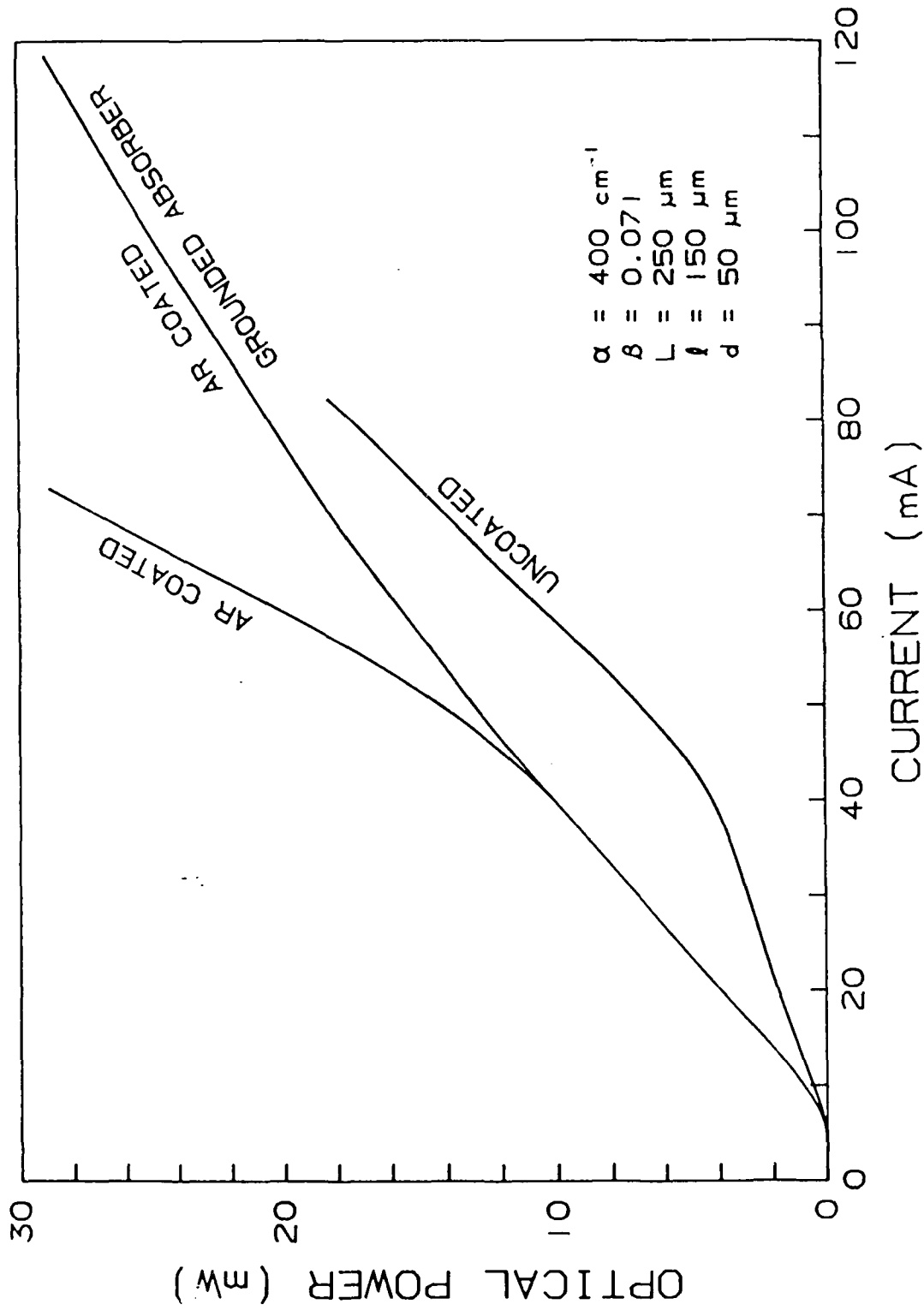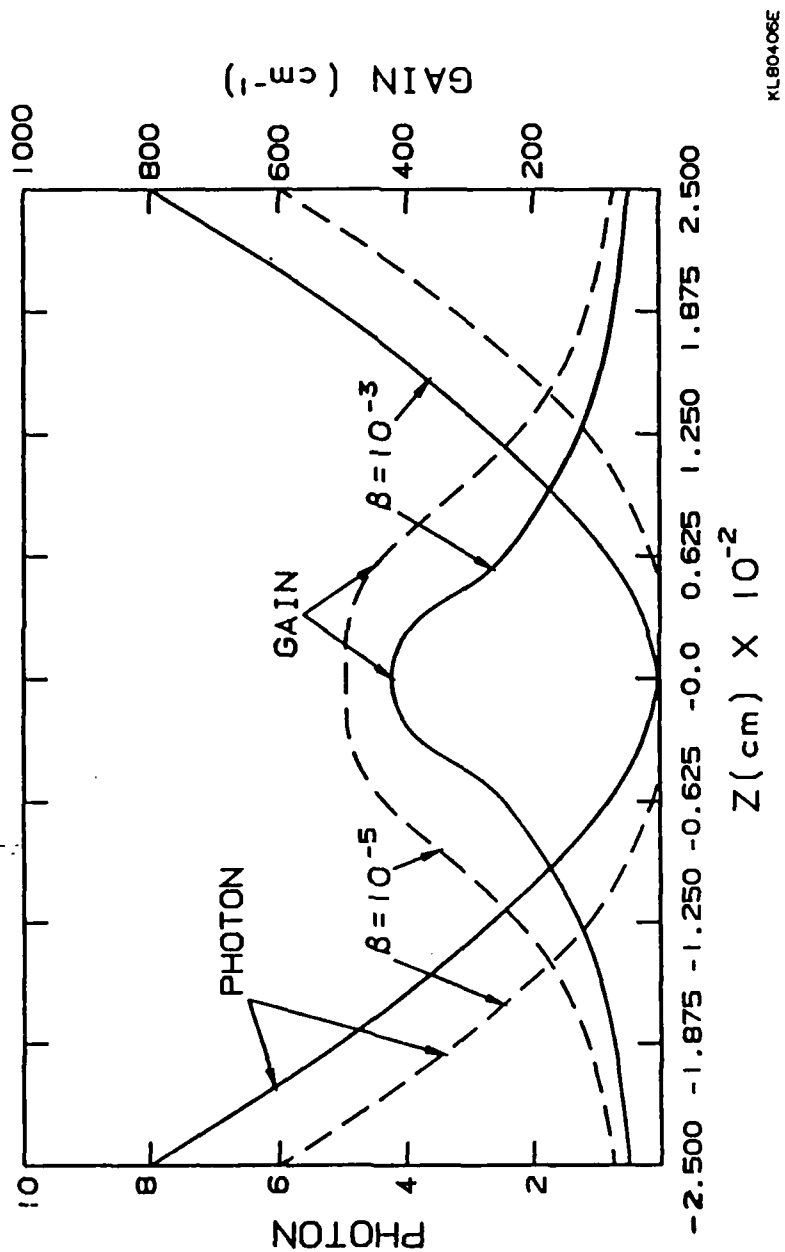
Fig. 13: Theoretical curves of the output power versus current for the three cases: (1) uncoated and an open-circuit absorber, (2) AR coated and an open-circuit absorber, and (3) AR coated and a grounded absorber.

point. The reason for the high value of β of 0.07 (as compared to 10^{-3} for a typical laser) is that in a laser one considers spontaneous emission into a single mode, which occupies a spectral span of only about 4Å, while for an SLD the entire spontaneous emission spectrum has to be included. The spontaneous emission factor in this case is governed mainly by geometric factors, namely the fraction of radiation emitted by an isotropic emitter captured by the waveguide. A strong waveguide like a buried heterostructure, in additional to having a high optical confinement factor and low carrier leakage, is particularly well suited for high efficiency SLD operation due to a high β. Figure 14 shows the actual spatial distribution of the electrons and the forward and backward propagation photon densities along the length of the diode. The linear region is the saturated superluminescent regime, where every electron injected into the active region is converted by stimulated emission into a photon.

4. The integrated modulator-superluminescent diode (MSLD)

The structure of the MSLD which we fabricated is shown in Fig. 1a. Comparing this with the standard SLD design (Fig. 1b), an extra section is added which can be pumped separately and acts as an optical modulator. The basic device structure is based on the SLD design as described above. Typical device dimensions are:

Fig. 14: Longitudinal distribution of carriers and forward and backward photons along the length of the SLD.

length of the pumped region L=300μm; the grounded absorber region l=250μm; the gap between the pumped and the grounded absorber region d=50μm; and the modulator region, t=100μm.

4.1 Device Perfomance

The light-current characteristic of a standard SLD shows a double "threshold" as shown in Fig. 15. The first threshold is interpreted as the onset of the superluminescent mode of operation as discussed in the last section. The emission spectrum displays a characteristic superluminescent structure. The spectral modulation defined as $m=(I_{max}-I_{min})/(I_{max}+I_{min})$ at the peak of the spectrum should be of a small value for SLD operation.

For the MSLD operation, the back absorber is grounded, and the voltage (current) into the front modulator section is varied. Fig. 16 shows the light emission from the front (modulator) facet as a funtion of the pump current into the middle gain section I_g, for various pump currents into the modulator section. The optical intensity can be varied by a factor of 3:1. The reason that the optical output cannot be totally extinguished, despite a large negative bias on the modulator, is that the modulator section in this device is relatively short and hence it is relatively easy for the superluminescent radiation to partially burn through the modulator. A longer modulator section should be able to offer a much higher extinction ratio.
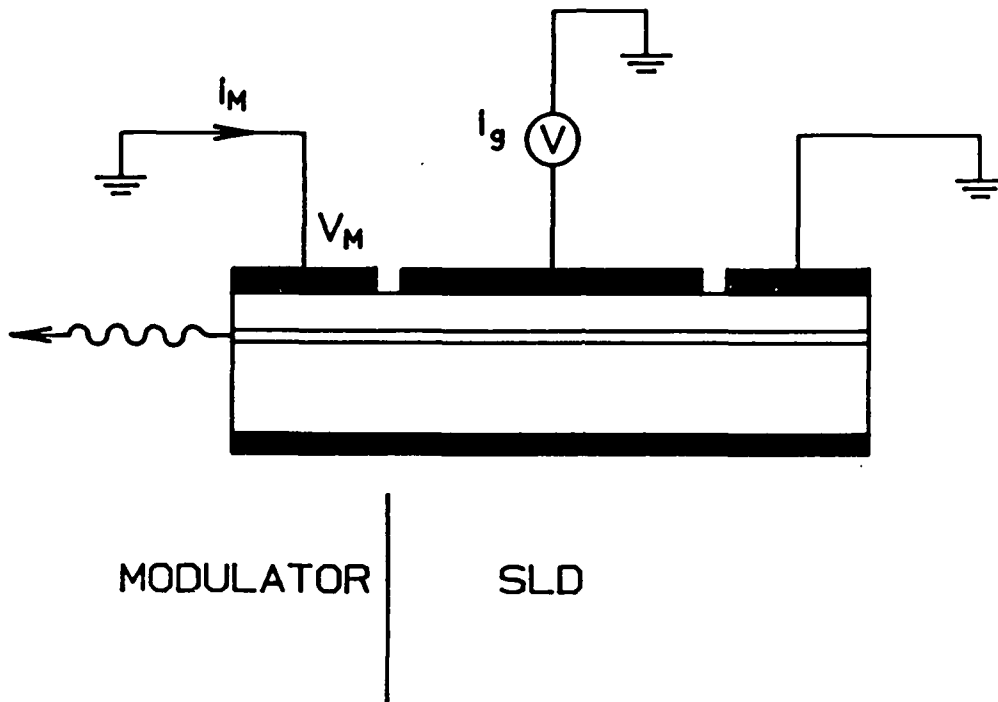
MODULATOR | SLD

KL80222C

Fig. 15: (a): Schematic diagram of the window buried heterostructure SLD, (b): an integrated modulator-SLD (MSLD).
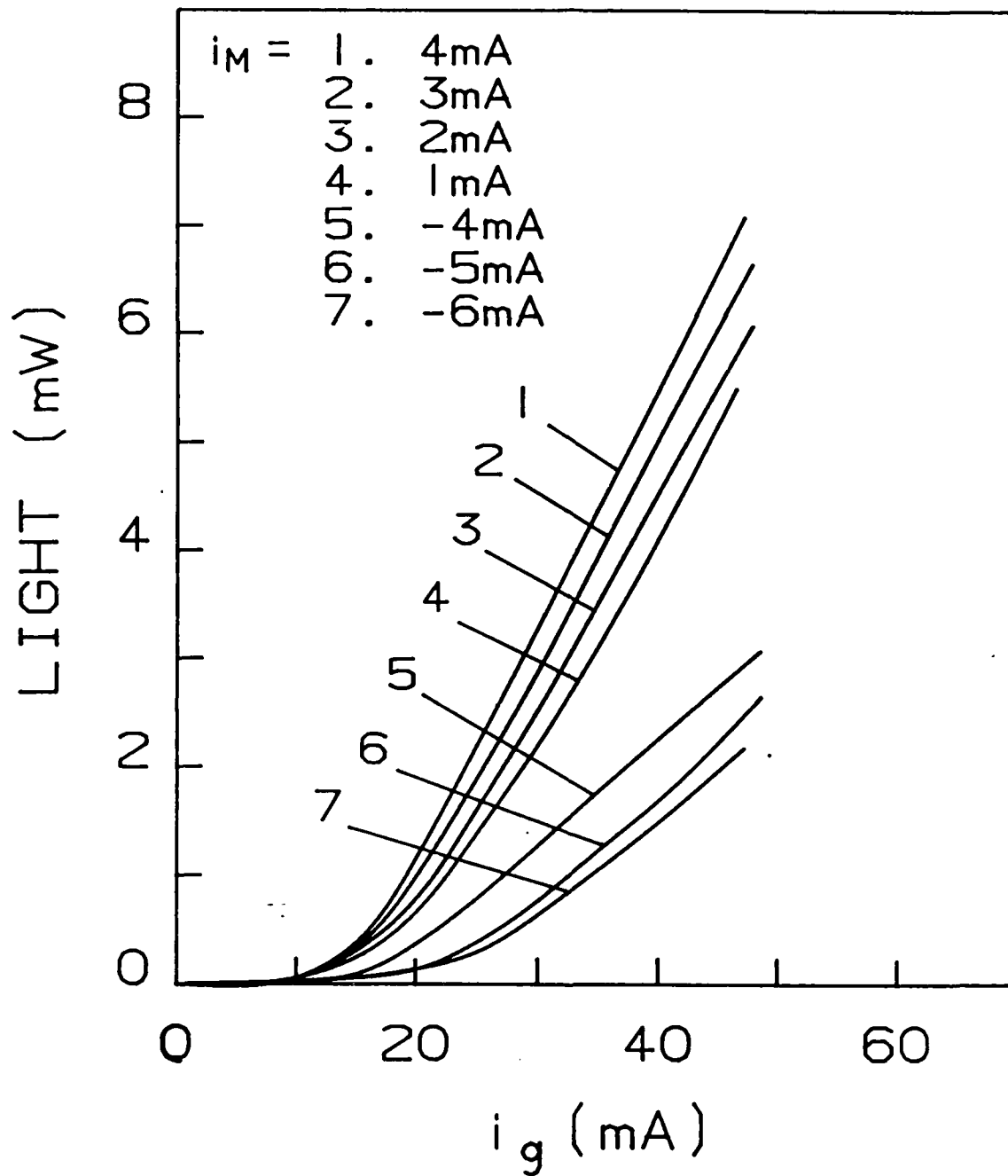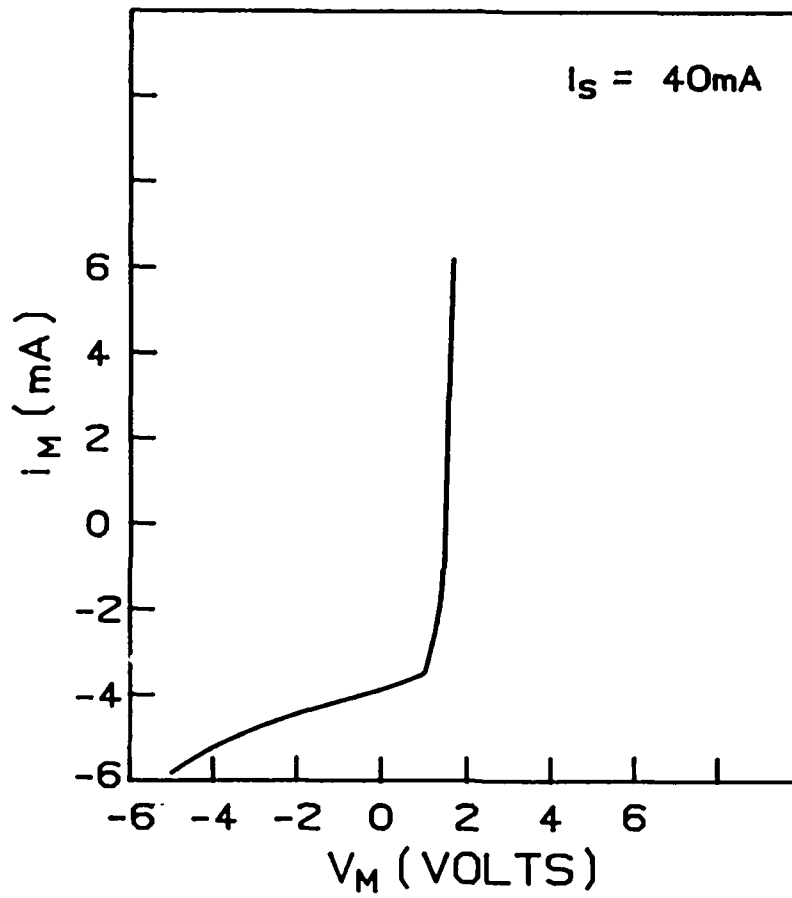
Fig. 16: Light output from the MSLD as a function of injection current into the gain section, for various bias currents into the modulator section.

The current-voltage characteristic of the modulator section at a constant current into the gain section is shown in Fig. 17. For bias voltage below 1.4V, the turn-on voltage of the GaAs pn-junction, a negative current flows as a result of the absorption of superluminescent radiation. As the negative bias voltage is increased, the amoung of absorption increases and results in a larger photocurrent and a higher extinction of the front facet output.

The modulator function is shown in Fig. 18, which is a plot of the light output from the front facet versus the current into the modulator section. An optical extinction ratio of 3:1 can be obtained with a change of injection current into the modulator section of only 0 -> -6mA. For the same amount of change in the superluminescent emission the injection current into the gain section have to be varied by >20mA. The modulator thus offers a highly efficient way of modulating the output of an SLD.

4.2 Analysis of MSLD

The analysis of the MSLD can in principle follow that of the SLD analysis in Section A-2, where we now have to match boundary conditions over four boundaries. Considerable simplication can be made if we assume that the front facet anti-reflection coating of the MSLD is near perfect, so that whether the modulator is in the ON or OFF state, the operation of the SLD is not affected. Under this circumstances the operation of the SLD can be described

$I_S = 40mA$

KLB0222E

Fig. 17: The voltage-current characteristic of the modulator section.
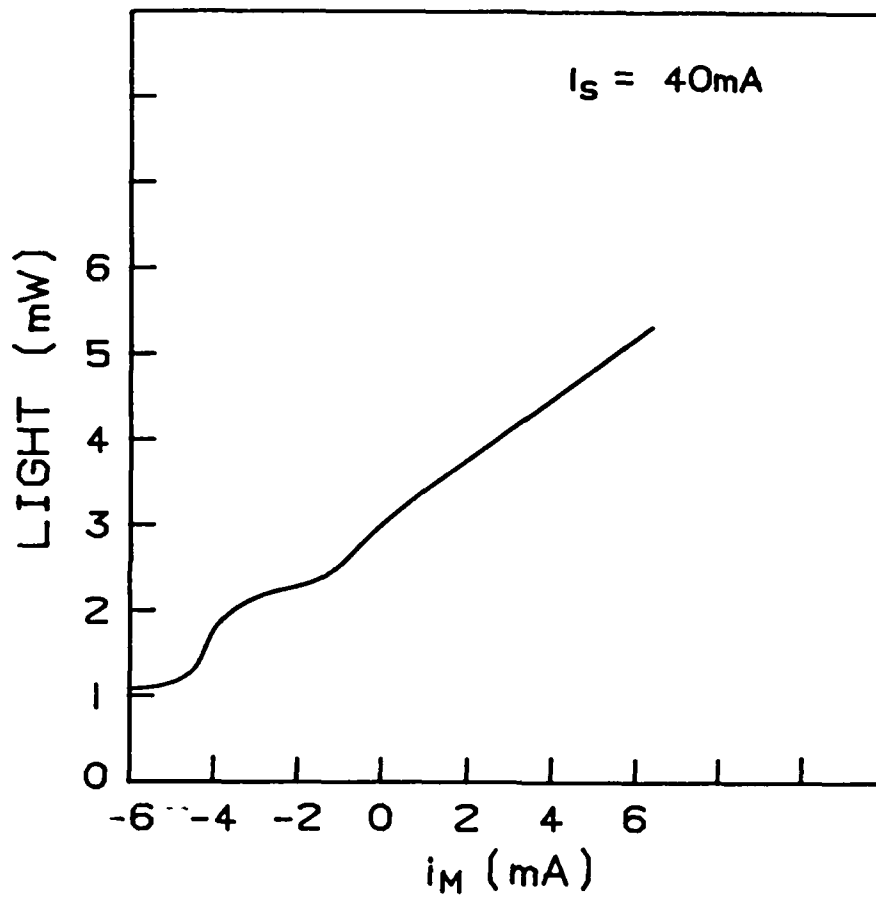
Fig. 18: Optical output from the MSLD as a function of the injection current into the modulator section.

quite independently of the modulator section and we can use the results directly from the above SLD analysis. Thus we can assume a fix optical input into the modulator section, and we would like to obtain the optical output from the modulator section as a function of the injection current into this section. Since we have assumed that the front facet coating is perfectly antireflection, we can make a futher simplification based on the fact that there will be very little backward travelling photons in the modulator section. Thus the propagation of the forward propagating photons in the modulator section can be described by

$$\frac{dX^{+}}{dz} = \kappa\left(N - N_0\right)X^{+} \tag{27}$$
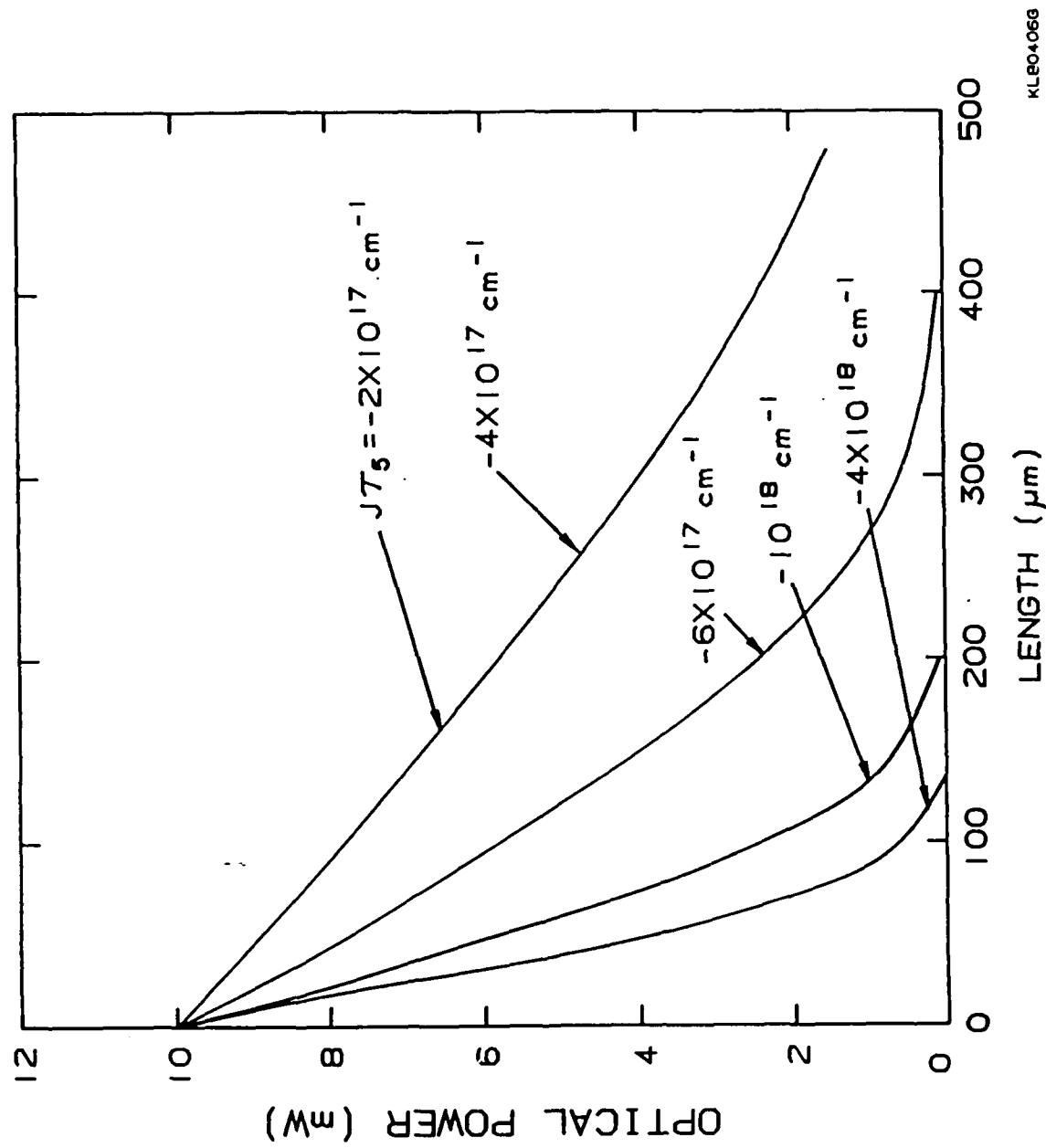
where the electron density is given by

$$\frac{N}{\tau_s} + \kappa c\left(N - N_0\right)X^{+} = J \tag{28}$$

where J is the pump current into the modulator section. Equations (27,28) can now be solved easily given an input photon density at z=0. The solution is

$$\ln\left(\frac{X^{+}}{P}\right) + \kappa c \tau_s\left(X^{+} - P\right) = \kappa\left(J\tau_s - \frac{N_0}{\tau_s}\right)z \tag{29}$$

where P=X^{+}(0) is the input photon density in the modulator section. A plot of X^{+} versus z at different values of J is shown in Fig. (19). The output of the modulator is given by X^{+}(L) where L is the length of the modulator. The modulation efficiency of the modulator is given by dX^{+}(L)/dI where I=JL is the total

Fig. 19: Profile of the forward propagating photon density in the modulator section as a function of the reverse current into the section.

injection current into the modulator section. We notice from Fig. (19) that unless one goes to a very high modulation depth, the linear term in Eq. (29) dominates. One can then neglect the logarithmic term in Eq. (29) and obtain an approximate expression for the modulation efficiency η:

$$\eta = \frac{dX^{\cdot}(L)}{dI} = \frac{1}{c} \tag{30}$$

This represents the situation that every electron entering the modulation section is responsible for absorbing a photon, and represents the highest possible efficiency for the modulator. This efficiency is, by the way, the same as that of an SLD in the saturated superluminesent regime, which is the linear region in the spatial distribution of the photon densities in an SLD as shown in Fig. (14). Thus one can see the advantage of modulating only the end region versus modulating the entire length of the SLD (the former is exactly the case in an MSLD), since injection of carriers into the middle portion of the SLD contributes to carrier loss by spontaneous emission instead of acting out the useful role of absorbing or emitting photons to providing optical modulation.

5. High speed modulation

5.1 SLD

To analyse the high speed modulation performance of an SLD, we use the local rate equations for the photon and electron densities as introduced in Section 2.2. For simplicity we will assume that the absorber section behaves as an infinite sink of photons, i.e., we assume a zero reflectivity at the absorber interface. Furthermore, we assume that the front mirror reflectivity is also zero. We then consider the dynamics of the gain (superluminescent) section. We use a perturbation expansion of the steady state solution:

$$X^*(z,t) = X_0^* + x^*(z)e^{i\omega t} \tag{31a}$$

$$N(z,t) = N_0(z) + n(z)e^{i\omega t} \tag{31b}$$

where $X^{+/-}$ are the forward and backward propagating photon densities, X_0's are the steady state distributions, and $x^{+/-}$ are the small signal modulation of the forward and backward modulations. We have assumed that the electron and photon densities throughout the length of the diode vary in unison. This is true when propagation effects are not important, i.e., when the modulation frequencies are small compared with the inverse of the photon transit time. This would amount to over 15GHz even for very long diodes (0.25cm).

Appling the usual small signal technique of substituting Eq. (32) into the superluminescent equations and neglecting the nonlinear product terms, we obtain the following small signal equations:

$$\frac{dx^+}{dz} = Ax^+ + Bx^- + C \qquad\qquad (33a)$$

$$\frac{dx^-}{dx} = Dx^+ + Ex^- + F \qquad\qquad (33b)$$

where A,B,C,D,E,F are given by the following:

$$A = g_0 - \frac{i\omega}{c\tau_s} - \frac{(X_0^+ + \beta)g_0}{1 + i\omega + (X_0^+ + X_0^-)} \qquad\qquad (34a)$$

$$B = -\frac{(X_0^+ + \beta)g_0}{1 + i\omega + (X_0^+ + X_0^-)} \qquad\qquad (34b)$$

$$C = \frac{(X_0^+ + \beta)g_m}{1 + i\omega + (X_0^+ + X_0^-)} \qquad\qquad (34c)$$

$$D = \frac{(X_0^- + \beta)g_0}{1 + i\omega + (X_0^+ + X_0^-)} \qquad\qquad (34d)$$

$$-E = g_0 - \frac{i\omega}{c\tau_s} - \frac{(X_0^+ + \beta)g_0}{1 + i\omega + (X_0^- + X_0^-)} \qquad\qquad (34e)$$

$$F = \frac{(X_0^- + \beta)g_m}{1 + i\omega + (X_0^+ + X_0^-)} \qquad\qquad (34f)$$

where $g_0(z) = \alpha N_0(z)$ = small signal gain distribution, $g_m = \alpha j\tau_s/ed$ = small signal gain due to RF pump current, and ω has been normalized by the inverse of the the spontaneous lifetime.

The boundary conditions for solving Eq. (33,34) are the same as that in solving the steady state:

$$x^+(0) = x^-(0) \qquad\qquad (35)$$

$$x^-(L/2) = 0 = x^+(-L/2) \qquad\qquad (36)$$

where we have assumed that the extent of the device is from -L/2

to +L/2. Equation (33-36) are solved by assuming an arbitrary value for $x^+(0)=x^-(0)=\kappa$ and integrating Eq. (33) to give $x^-(L/2)=P$, $x^-(L/2)=Q$, these quantities are ocmplex in general. The system Eq. (33) is integrated again assuming $x^+(0)=x^-(0)=\rho \neq \kappa$ to give $x^+(L/2)=T$, $x^-(L/2)=S$. The solution is given by a suitable linear combination of the above two solutions such that $x^-(L/2)=0$. The small signal output of the superluminescent diode is

$$x^*(L/2) = x^-(-L/2) = \frac{QT - SP}{Q - S} \tag{37}$$

The frequency response curve is obtained by solving Eq. (33) for each ω. One set of results is shown in Fig. (20) where we show the frequency response of a 500μm diode pumped to various levels of unsaturated gain. The sponteneous emission factor β is taken to be 10^{-4} and this choice of a small spontaneous emission factor is responsible for the high modulation bandwidth observed. This is abundantly clear when we plot the frequency response of a 500μm diode pumped to an unsaturated gain of 500cm^{-1} , at different values of β as shown in Fig. (21). At the realistic values of β >10^{-2} , the direct modulation response falls to around 1GHz, which is what we observed experimentally as shown in Fig. (22). Thus, while the high spontaneous emission is responsible for a high SLD power as discussed in Section 3, it at the same time
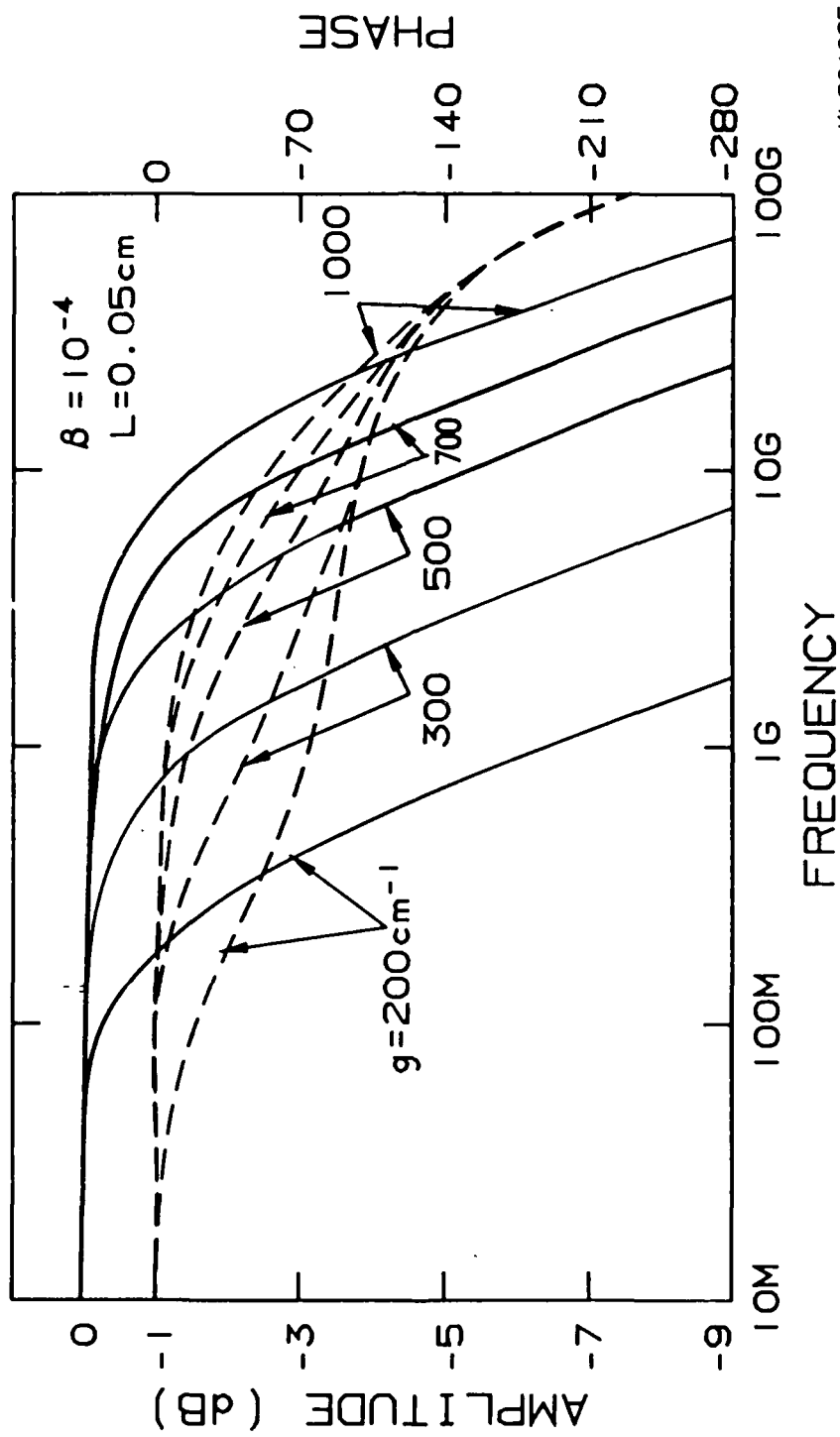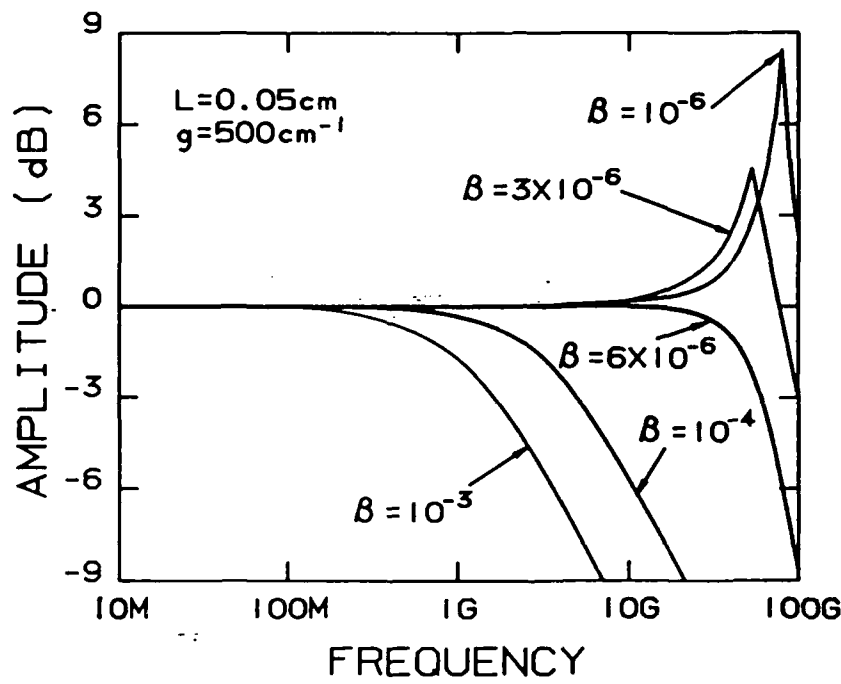
52

Fig. 20: Amplitude modulation response of an SLD at various injection levels.

Fig. 21: Modulation response of a SLD with various values of β.

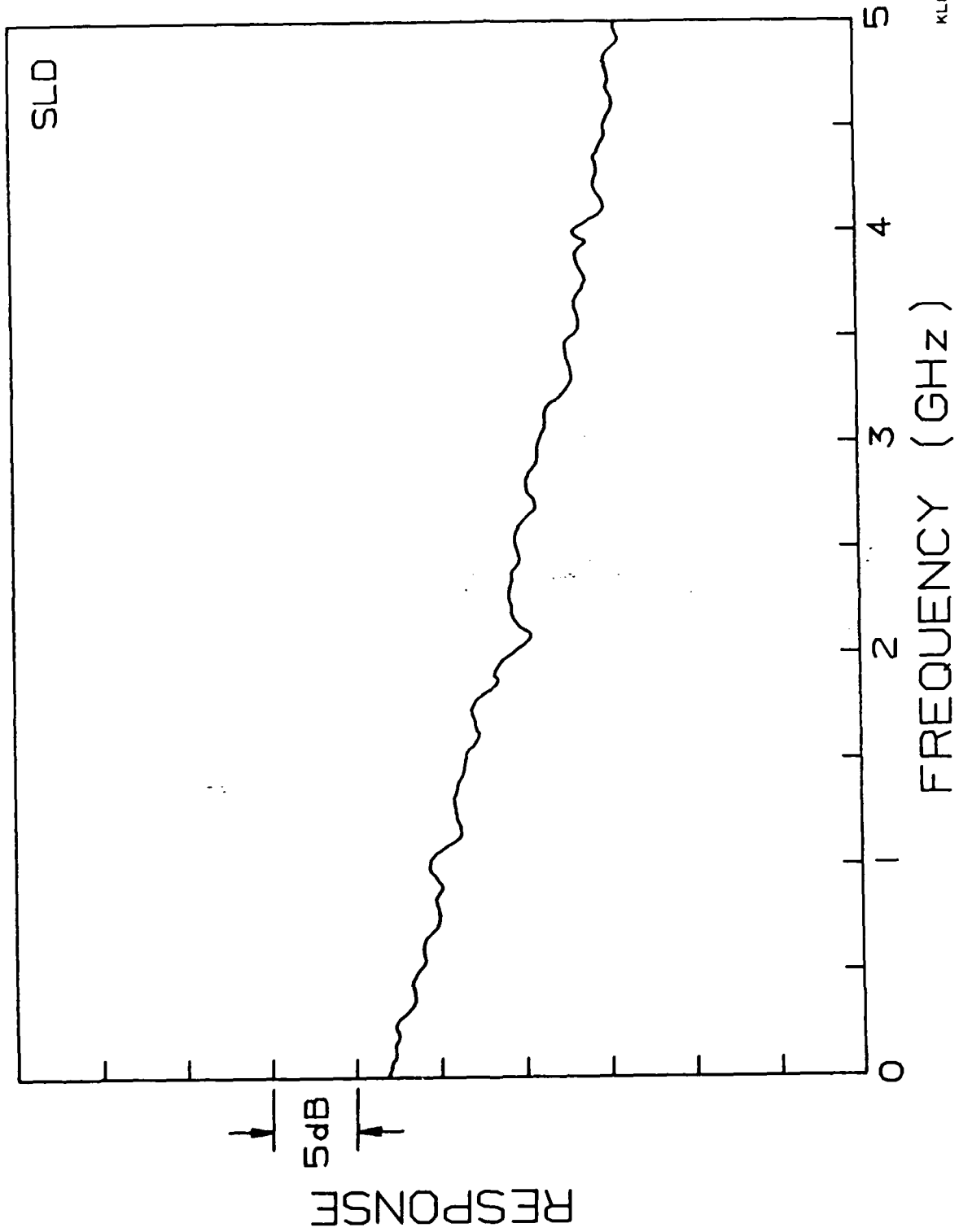Fig. 22: Experimental direct modulation response of an SLD.

KL80406A

limits the direct modulation bandwidth. One can in principle trade off bandwidth with power with a proper design for the value of β.

5.2 MSLD modulation

Experimental results of the direct modulation of the MSLD is shown in Fig. 23. The results looks very similar to the direct modulation result of the SLD. The direct modulation response of the MSLD can in principle be analysed using the approach described above. However, in the case of the MSLD, considerable simplification can be made if one neglects the spatical dependence of the photon distribution and perform a "mean-field" analysis. The transmission of the optical radiation through the modulator depends on the electron density in the modulator. The dynamics of the electron density variation is governed by the following rate equation:

$$\frac{dN}{dt} = J - A(N - N_0)P - \frac{N}{\tau_s} \tag{38}$$

where A is the "differential gain constant" which is related to the gain constant κ above by $A=\kappa c$. In a typical operation of the modulator, a reverse bias is applied for the OFF state, in which case the electron density is held at a low value much below that for transparency. To turn the modulator ON, one would inject current into the active region to bring the device to transparency. It is obvious from Eq. (38) that the governing time
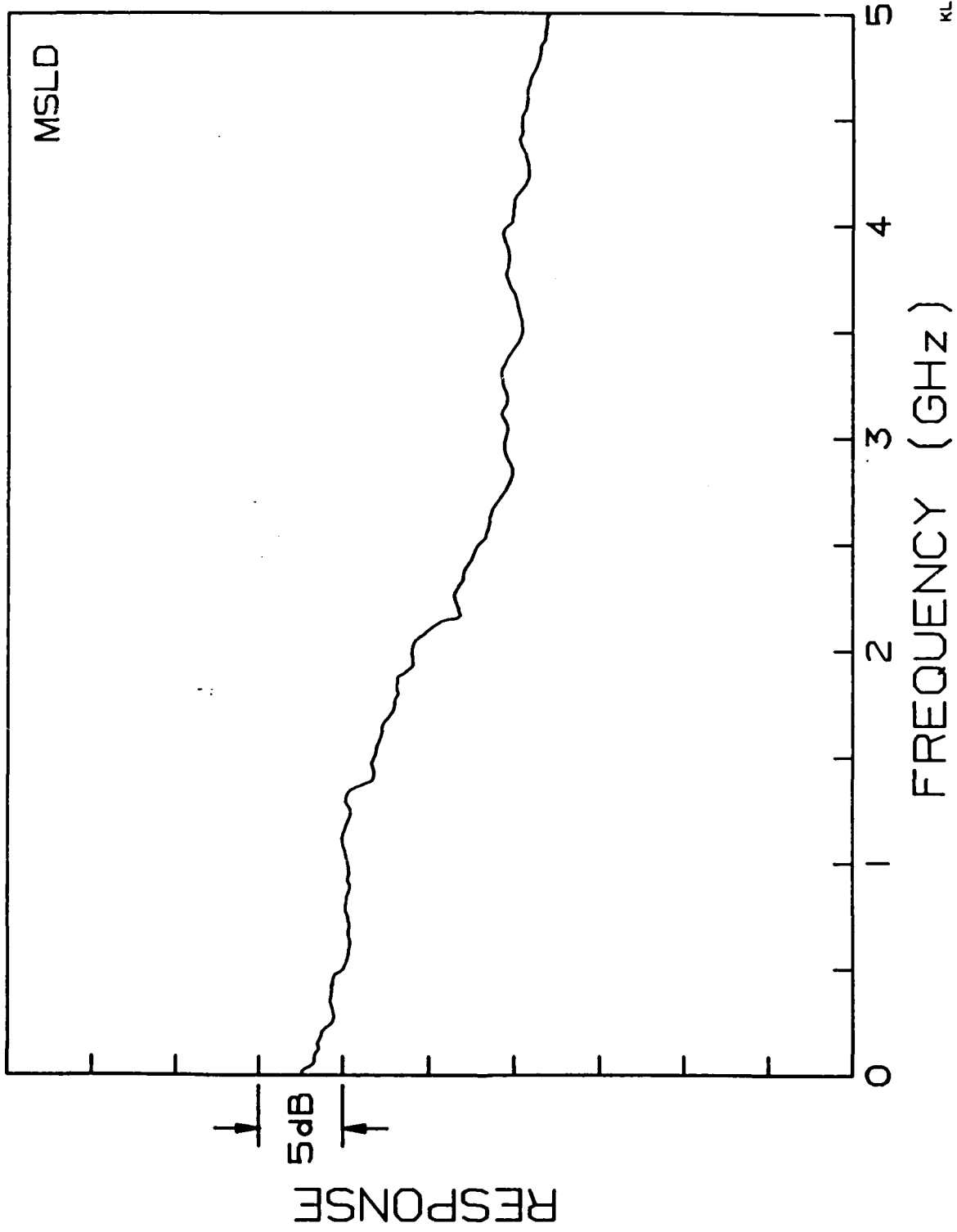
Fig. 23: Experimental direct modulation response of an MSLD.

constant is the stimulated lifetime of the carriers, $\mu_{stim}=1/AP$. For typical optical powers of a few milliwatts, the stimulated lifetime is a fraction of a nanosecond, which translates to a modulation bandwidth of slightly above 1GHz. It is also obvious that increasing A can directly enhance the modulation bandwidth. This issue will be taken up below. A second speed-determining factor is the transparency electron density N_O . For a device with a low transparency density, a small current pulse can rapidly charge the device up from the OFF level to the ON level. Thus a low transparency density and a high differential gain constant are both needed for high speed operation of an MSLD. It turns out that quantum well materials can satisfy both criteria, as the discussion in the following section will show.

6. Quantum well materials as superluminescent/modulator media

6.1 Quantum well structures

A quantum well structure consists of a very thin active layer, 100Å or less, in which the motion of electrons in the direction perpendicular to the well are confined to less than a de Broglie length and the allowable energies are quantized into distinct levels. The most important consequence of this quantization is the modification of the "density of states" function into a staircase-like characteristic (Fig. 24). As one starts to pump electrons into a quantum well, the electron density builds up to a point where the material becomes optically transparent, and

QUANTUM WELL DENSITY OF STATES
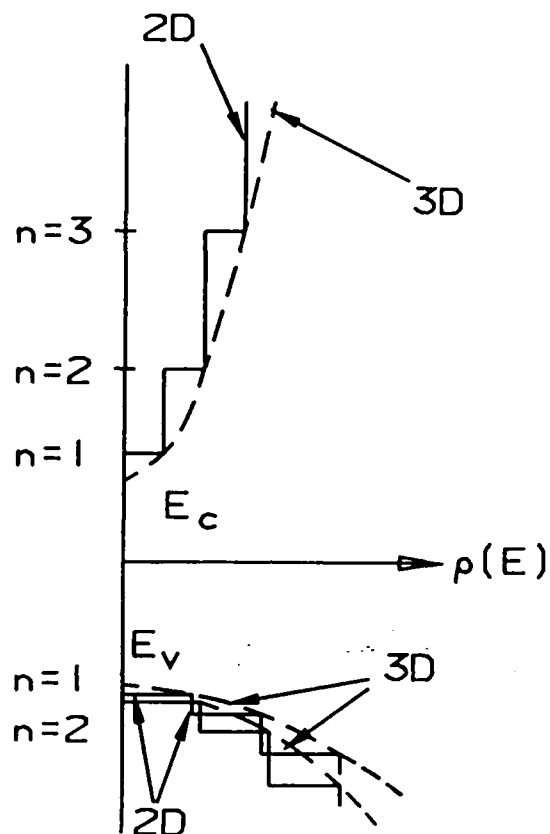
$$\rho_j(E) = \frac{m_j}{\pi \hbar^2 L_z} \left\{ \text{Int} \left[\frac{E - E_j}{E_{n,j} - E_j} \right]^{\frac{1}{2}} \right\}$$

$$j = C, \ H, \ L$$

KLB0406H

Fig. 24 Density of states of a quantum well.

further increase in electron density brings about optical gain. The optical gain is considerably higher in a quantum well than in conventional bulk material, but since its small physical dimension results in a very weak confinement of the optical mode, there is **NO** substantial overall advantage in a single quantum well as far as optical gain is concerned. The problem associated with a small optical confinement in quantum wells can be circumvented by using multiple quantum wells in the active region of a laser. On the other hand, since the electron density for transparency in a quantum well is approximately the same as that in bulk material, the small physical dimension of the former implies that a very tiny injection current is sufficient to bring it to transparency.

A significant result of the above discussion is that while a **single** quantum well laser does not have a very high optical gain, the transparency condition can be most easily reached compared to conventional or multiquantum well structures. On the other hand, a multiquantum well structure can offer high optical gain as well as high differential optical gain, but has a higher value for transparency. Thus depending on the exact design of the transmitter driving electronics, there can be tradeoffs in the design of the MSLD.

6.2 Theoretical explanation of quantum well gain/absorption

A simple model can be used to describe the essential characteristics of quantum well gain and absorption and their implications on efficiency and modulation speed of the MSLD. The one dimensional carrier confinement in a quantum well leads to a staircase density of states function. The modal gain at photon energy E can be calculated from

$$g(E) = C \sum_i H\{(E - E_g)S - E_n\}\{2f_c(E) - 1\} \qquad (39)$$

The constant C, the maximum available modal gain per quantized state, is estimated from gain measurement data to be $100 cm^{-1}$. The conduction band offset as a fraction of the total bandgap offset, S, is taken to be 0.85. The staircase nature of the density of states function is represented by the Heaviside function H. For E_g we use the bandgap energy of bulk GaAs which is 1.4eV. The Fermi function for the electrons with the quasi Fermi energy E_{fc} is

$$f_c(E) = \frac{1}{\exp(((E - E_g)S - E_{fc})/kT) + 1} \qquad (40)$$

With $m_c* = 0.067 m_e$ where m_e is the electron mass, a 100A infinite wall well implies that the first quantized energy is $E_1 = 0.056eV$ and that E_2 is foru times as large. The expression Eq. (39) is a slight simplification that ignores some of the specific hole features and does not include collision broadening.

Figure 25 shows the electron density distribution and gain spectrum for two conditions: (a) is for the case of a low pump current density (b) is at a higher current density. The gain
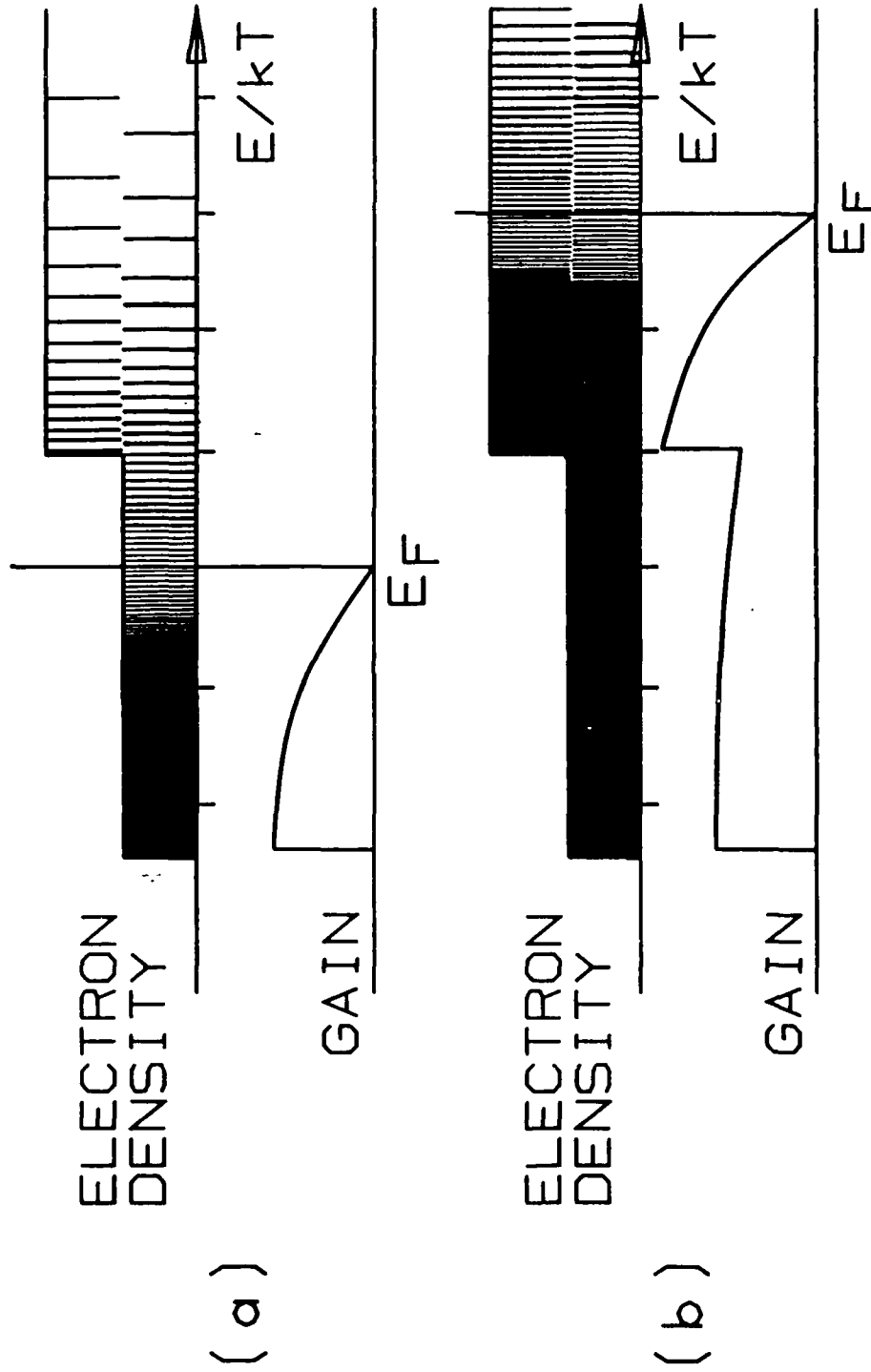
Fig. 25 Schematic diagram of occupation of the staircase density of states in a quantum well and the associated gain spectrum due to filling of electrons.

spectrum at the higher pumping level is very wide and shows a new peak at the onset energy of the second quantized state. Especially notable is the doubling of the gain at the onset energy of the second quantized state where its gain adds to that of the first one. Also notice the very steep rise in the gain, which means a very high differential gain constant, at the beginning of the curve. Since the modulation speed of the device is dependent on the differential gain, this high differential gain contributes to the high speed advantage of the quantum well devices. Furthermore, considerably higher quasi-Fermi energies lead to nearly double the gain in the high energy region with respect to the maximum value obtainable from the n=1 state alone.

For more realistic quantitative results, broadening is incorporated via an effective smearing of the steps in the density of states function in the basic model by an amount $\Delta E = h/(2\Pi\tau)$ where τ is the intraband scattering time of the electrons. A value of $\Delta E = 6.6$meV corresponding to $\tau = 0.1$ps is used. The broadening is altered to have exponential tails rather than a Lorentzian shape. Including broadening, the modal gain expression becomes

$$g(E) = C \sum_n \frac{1}{\exp\left(\left(E_n - E\right)S/\Delta E\right) + 1} \left\{2f_c(E) - 1\right\} \qquad (41)$$

This equation gives gain spectra as shown in Fig. 26 for different quasi Fermi energies. In this model the gain curve crosses zero at the quasi-Fermi energy of the conduction
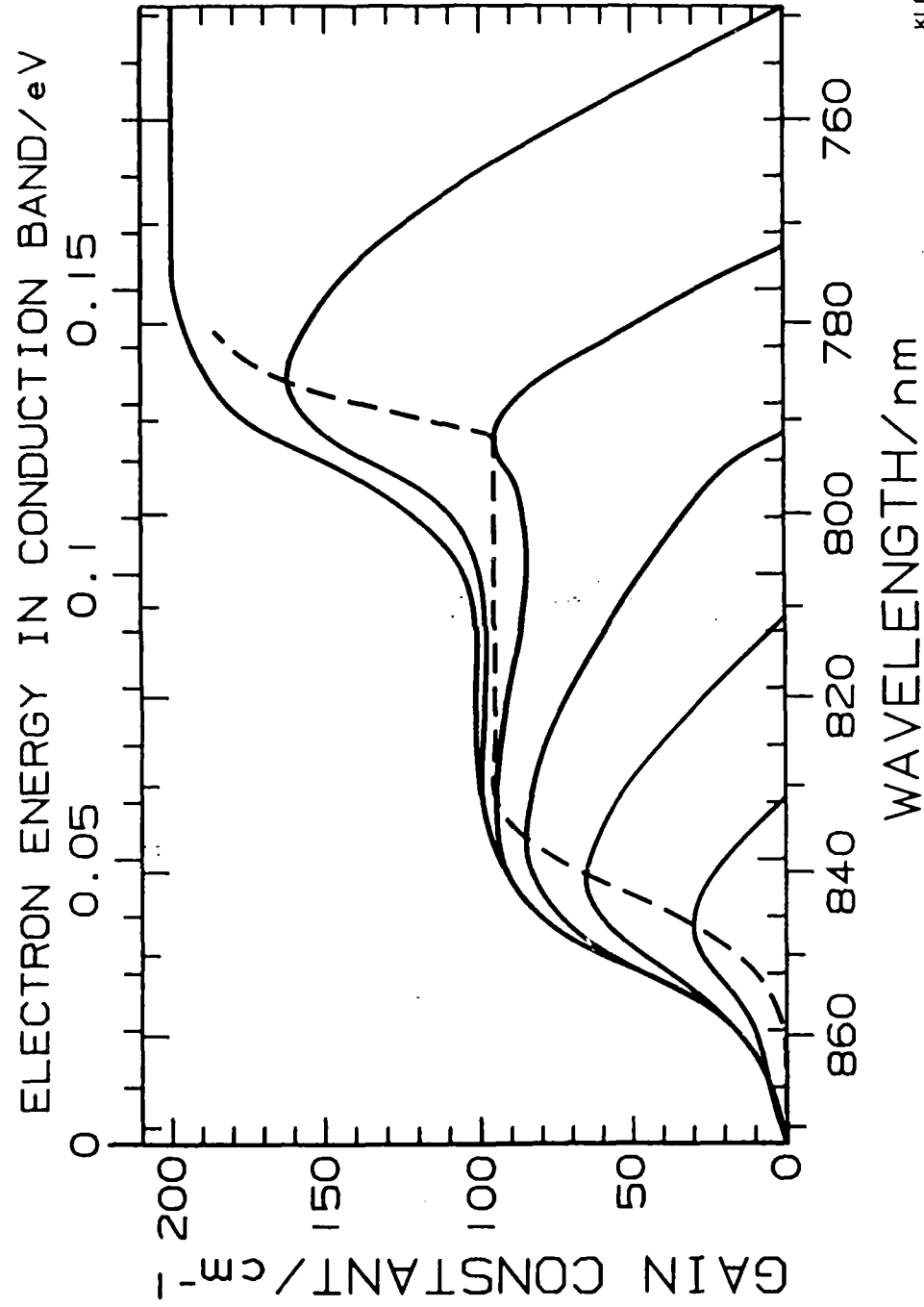
Fig. 26   Calculated gain spectrum for various injection levels.

KLB0406C

electrons. The higher quasi-Fermi energies (corresponding to higher pump densities) are associated with the short cavity lasers. The results show a wide gain spectrum which leads to a high level of recombination radiation even as threshold is approached.

The uppermost curve in Fig. 26 shows the maximum available gain as a function of photon energy, that is, the value which would result from an infinite pumping current in this model. Therefore the gain needed to overcome very high losses can only be obtained from a SQW laser by enlisting the added contribution of a second quantized state. By tracking the peak of the gain spectrum for varying quasi-Fermi energies as indicated in Fig. 26 the optical gain as a function of injection current can be obtained as shown in Fig. 27. What this shows is that a single quantum well does not offers a lot of gain, but can be made to be transparent very easily and the optical loss of the structure is very low. On the other hand, multiquantum well lasers can offer very high gain as well has higher differential gain throughout the range of operation current, but needs a higher electron density to become transparent. It is not immediately clear which one is more suitable for fabrication of SLD/MSLD, the result awaits further analysis.
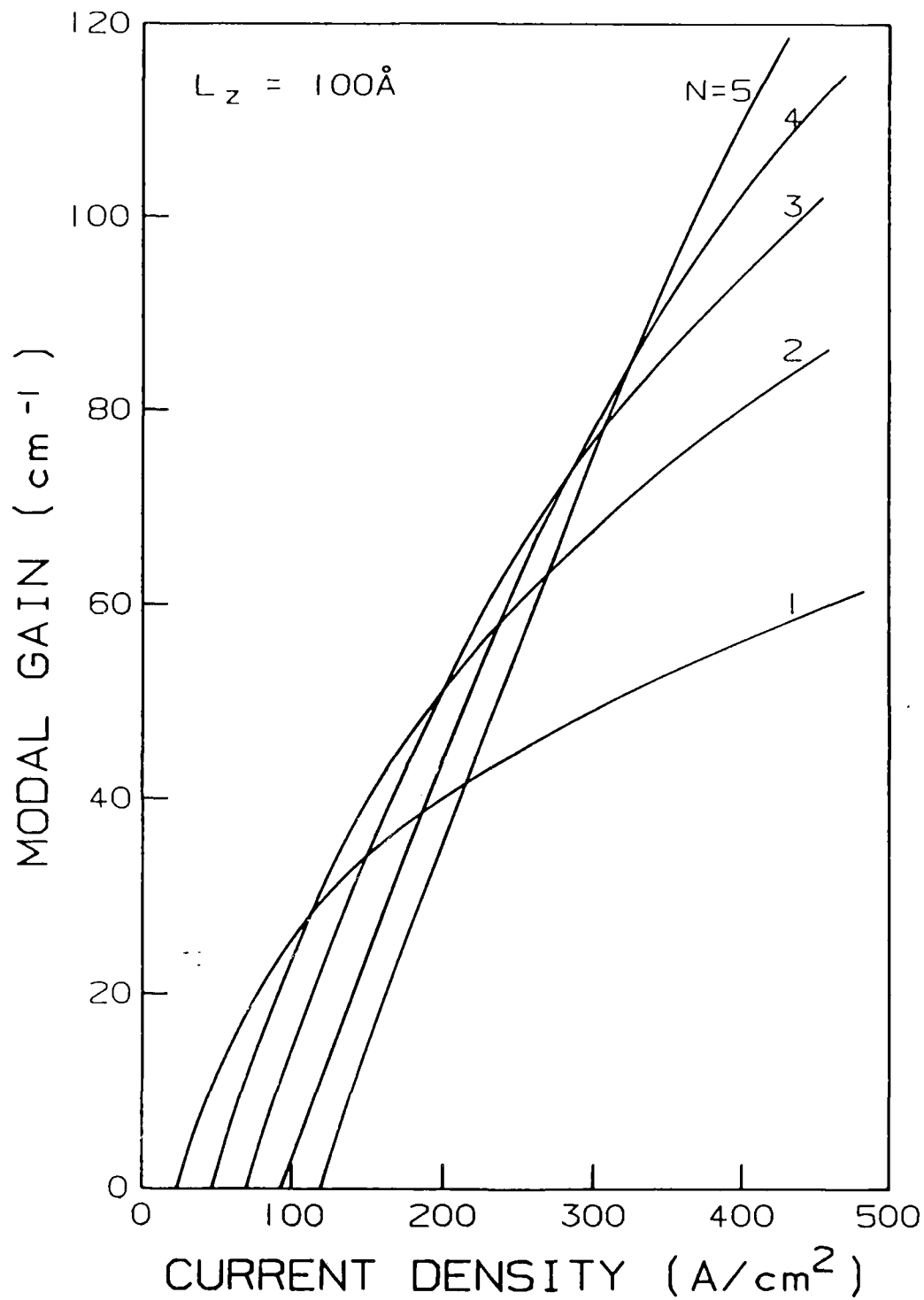
Fig. 27 Calculated peak gain as a function of injection current density for single and multiple quantum wells.

7. References:

1. P.L. Derry, A. Yariv, K.Y. Lau, N. Bar-Chaim, K. Lee and J. Rosenberg, Appl. Phys. Lett., **50**, 1773, 1987.

2. K.Y. Lau, N. Bar-Chaim, P.L. Derry, A. Yariv, Appl. Phys. Lett., **51**, 69, 1987.

3. K.Y. Lau, P.L. Derry, A. Yariv, Appl. Phys. Lett., **52**, 88, 1988.

4. K. Ogawa, IEEE J. Quant. Electron., **QE-18**, 849 (1982).

5. T.P. Lee, C.A. Burrus, and B.I. Miller, IEEE J. Quantum Electron. **QE-9**, 820,1973.

6. C.S. Wang, W.H. Cheng, and C.J. Huang, W.K. Burns, and R.P. Moeller, Appl. Phys. Lett., **47**, 587, 1982.

7. I.P. Kaminow, G. Eisenstein, L. Stulz, and A.G. Dentai, IEEE J. Quantum Electron. **QE-19**, 78, 1983.

8. T.L. Paoli, R.L. Thornton, R.D. Burnham, and D.L. Smith, Appl. Phys. Lett. **47**, 450, 1985.

9. I.P. Kaminow, G. Eisenstein, and L. Stulz, IEEE J. Quantum Electron. **QE-19**, 493, 1983.

10. G. Eisenstein and L.W. Stulz, Appl. Opt. **23**, 161, 1984.

11. G. Eisenstein, L.W. Stulz, and L.G. Van Uitert, J. Lightwave Technol. **L.T.-4**, 1373, 1986.

12. N.K. Dutta and P.P. Deimel, IEEE J. Quantum Electron. **QE-19**, 496, 1983.

13. J. Niesen, P.H. Payton, C.B. Morrison, and L.M. Zinkiewiez, paper Tu C2 presented at Southwest Optics Conference, Albuquerque, New Mexico, Feb. 9-12, 1987.

14. G.A. Alphones, D.B. Gilbert, M. Harvey, E. Depiano, and M. Ettenberg, paper ME6 presented at the Optical Fiber Communication Conference, Reno, Navada, Jan., 1987.

15. K.Y. Lau, N. Bar-Chaim, I. Ury, and A. Yariv, Appl. Phys. Lett. **45**, 316, 1984.

16. H.C. Casey, Jr and M.B. Panish, "Heterostructure Lasers", part A, p. 172, Academic Press, New York, 1978.

END
DATED
FILM
8—88
DTIC